Quaternary Science Reviews 383 (2026) 109922

Contents lists available at ScienceDirect

Quaternary Science Reviews

journal homepage: www.elsevier.com/locate/quascirev

Invited Paper

Oceanographic and climatic controls of meteoric ^{10}Be fluxes to seafloor sediments: A global synthesis

Jennifer Middleton [a,*], Frank Pavia [b], Robert Anderson [a,c], Roseanne Schwartz [a], Martin Fleisher [a], Yong Lao [a,c], Yuxin Zhou [d], Christopher Kinsley [e], Joerg Schaefer [a,c], Martin Frank [f], Gisela Winckler [a,c]

[a] Lamont-Doherty Earth Observatory, Columbia University, Palisades, NY, 10964, USA
[b] School of Oceanography, University of Washington, Seattle, WA, 98195, USA
[c] Department of Earth and Environmental Sciences, Columbia University, New York, NY, 10027, USA
[d] School of Earth and Atmospheric Sciences, Georgia Institute of Technology, Atlanta, GA, 30332, USA
[e] Department of Earth, Atmospheric, and Planetary Sciences, Massachusetts Institute of Technology, Cambridge, MA, 02139, USA
[f] GEOMAR Helmholtz Centre for Ocean Research Kiel, Kiel, Germany

ARTICLE INFO

Handling Editor name: Carin Andersson Dahl

Keywords:
Beryllium-10
Excess thorium-230
Constant flux proxies
Ocean circulation
Paleoceanography
Particle scavenging
Atlantic Ocean
Southern Ocean
Pacific Ocean

ABSTRACT

Marine sedimentary beryllium-10 (^{10}Be) has been used to constrain many paleoenvironmental processes over the past 10 million years, but dynamic processes such as particle scavenging and ocean circulation can complicate interpretation of sedimentary ^{10}Be data. We generated six new sedimentary ^{10}Be flux records, normalized using excess thorium-230 ($^{230}Th_{XS}$), and present a global compilation of $^{230}Th_{XS}$-normalized ^{10}Be flux data combined with $^{230}Th_{XS}$-normalized bulk sediment flux and sediment composition data to improve constraints on the climatic and oceanographic factors governing ^{10}Be fluxes to the seafloor. Our analysis suggests that the first order factors driving global variability in sedimentary ^{10}Be fluxes are (1) bulk sediment flux; (2) sediment composition; and (3) a combination of ocean basin and sediment core water depth that likely reflects the overlying water mass concentration of ^{10}Be. While these parameters explain ~60-80% of the variance observed in the core top and Holocene data, the correlations exhibited between these parameters and ^{10}Be fluxes are much weaker in the 0-250 ka time series data. The increased variability observed in the time series data likely results from climatically-driven changes in the available seawater ^{10}Be inventory within each water mass over time, although we cannot rule out the impact of variable carbonate and opal dissolution. The sensitivity of abyssal sediment ^{10}Be fluxes to seawater ^{10}Be concentrations suggests that sedimentary ^{10}Be could be used to reconstruct past changes in basin-scale particle fluxes and ocean circulation, analogous to the shorter-lived protactinium-231 (^{231}Pa) and $^{230}Th_{XS}$ systems, throughout the Late Neogene and supports further refinement of ^{10}Be as a paleoceanographic proxy.

1. Introduction

Marine archives of meteoric beryllium-10 (^{10}Be), typically quantified as ^{10}Be fluxes or ^{10}Be/^{9}Be ratios in marine sediments and ferromanganese crusts, have been used to investigate a myriad of dynamic processes occurring within the last ten million years of Earth history. These applications include reconstructions of geomagnetic field intensity (e.g., Raisbeck et al., 1985; Frank et al., 1997; Christl et al., 2010; Simon et al., 2016a; Savranskaia et al., 2021), the influx of cosmic rays (Koll et al., 2025; Feige et al., 2013), continental weathering rates (von Blanckenburg and O'Nions, 1999; Willenbring and von Blanckenburg, 2010a), ice sheet meltwater and ice shelf conditions (Valletta et al., 2018; White et al., 2019; Sellén et al., 2009; Yokoyama and Sproson, 2026), seawater particle scavenging (e.g., Frank et al., 2000; Chase et al., 2002, 2003a), and ocean transport (Christl et al., 2007). In addition, the 1.39 Myr half-life of ^{10}Be (Chmeleff et al., 2010; Korschinek et al., 2010), has enabled its use to constrain age models for slow growing ferromanganese crusts and carbonate-poor sediments dating up to 12 Ma (e.g., Bourles et al., 1989; Frank et al., 2008; Koll et al., 2025).

The diverse utilization of ^{10}Be to constrain paleo processes arises from its unique isotopic and chemical behavior as it flows through a multi-step pathway from atmospheric production to deposition on the

* Corresponding author.
E-mail address: jennym@ldeo.columbia.edu (J. Middleton).

https://doi.org/10.1016/j.quascirev.2026.109922
Received 10 October 2025; Received in revised form 27 February 2026; Accepted 3 March 2026

seafloor. Meteoric ^{10}Be is produced in the atmosphere by cosmic ray induced spallation of nitrogen and oxygen and rapidly (<1 yr) transported to the Earth surface, primarily via wet deposition (Lal and Peters, 1967; McHargue and Damon, 1991). After deposition in the dissolved phase at the sea surface, this ^{10}Be is gradually removed by particle scavenging over timescales of ~200-1000 yr (Anderson et al., 1990; Ku et al., 1990; Kaste and Baskaran, 2012) and provides the dominant pathway of ^{10}Be to the underlying sediments (Kusakabe et al., 1987; McHargue and Damon, 1991). Although the atmospheric production and surface deposition patterns of ^{10}Be vary spatially (Lal and Peters, 1967; Heikkilae and von Blanckenburg, 2015; Deng et al., 2020), the residence time of ^{10}Be within the water column is thought to be sufficiently long to allow for relative homogenization of dissolved ^{10}Be concentrations within the deep waters of a given basin (Anderson et al., 1990; Kaste and Baskaran, 2012). Even within a single basin, however, dynamic ocean processes, such as assorted scavenging particle flux and composition, as well as water mass transport, can increase or decrease the sedimentary ^{10}Be flux relative to its rate of atmospheric production and sea surface deposition (Chase et al., 2002, 2003b; Christl et al., 2003).

Many paleo-environmental applications of ^{10}Be, such as constraining past geomagnetic field intensity or the influx of cosmic rays, rely on the ability to reconstruct the atmospheric ^{10}Be production rate signal from marine archives. However, the oceanographic and particle flux effects on seafloor ^{10}Be fluxes can vary dramatically within the paleorecord due to regional-scale climatic variability, thus introducing additional uncertainties to interpretations of production rate signals in sedimentary ^{10}Be data (Savranskaia et al., 2021; Frank et al., 1997). Rather than purely introducing "noise" into production rate reconstructions, the sensitivity of ^{10}Be to ocean transport and particle scavenging gives this isotope system great potential to further constrain global oceanographic conditions throughout the late Neogene. Yet, much remains unconstrained regarding the relative importance of these two processes in setting local water column ^{10}Be inventories and sedimentary ^{10}Be fluxes across different ocean basins and depositional environments (Deng et al., 2025; Frank et al., 2002; Chase et al., 2003a, 2003b; Christl et al., 2007; Savranskaia et al., 2024).

Scavenging particles are the primary removal agents of ^{10}Be from seawater to sediments and the composition and fluxes of these particles are important regulators of sedimentary ^{10}Be fluxes. Water column and sediment ^{10}Be studies suggest that ^{10}Be has a high affinity for scavenging (a high partition coefficient K_d) by biogenic opal and lithogenic particles and a low affinity for scavenging (low K_d) by calcium carbonate (Chase et al., 2002, 2003a; Frank et al., 2000; Lao et al., 1993; Kretschmer et al., 2011). Additional work on the short-lived cosmogenic isotope ^{7}Be indicates that the presence of organic carbon may also enhance the efficiency of Be scavenging by all particle types (Yang et al., 2015), although the impact of this effect on sedimentary ^{10}Be records is difficult to assess due to the poor preservation of organic matter in typical marine depositional environments. Perhaps because of its scavenging affinity for opal and organic matter, Be exhibits nutrient-like distributions in the ocean, with strong surface scavenging and deep-water regeneration (Kusakabe et al., 1990). Recent modeling work reproduced water-column ^{10}Be concentration data within a 34% model-data misfit using opal and particulate organic carbon scavenging alone (Deng et al., 2025). Over variable climatic conditions, changes in scavenging particle composition and the flux of particles to the seafloor can also impact resulting sedimentary ^{10}Be fluxes, although the exact nature of these changes appears to vary from site to site (Anderson et al., 1990; Frank et al., 1997, 2000).

Beyond the scavenging particles themselves, the concentration of dissolved ^{10}Be in the water column through which the particles descend plays a critical role in governing sedimentary ^{10}Be fluxes (e.g., Frank et al., 2002; Sellén et al., 2009). In turn, seawater ^{10}Be concentrations appear to be a function of ocean circulation, water mass and depth (von Blanckenburg et al., 1996; Frank et al., 2009; Segl et al., 1987; Measures et al., 1996; Kusakabe et al., 1987; Deng et al., 2025). In the open ocean, deep seawater measurements (>1000 m) appear to exhibit increasing ^{10}Be concentrations with increasing water mass age, or last contact with the atmosphere, along the circulation pathway from the North Atlantic to the Pacific (e.g., Deng et al., 2025 and references therein). Whether this phenomenon arises from the nutrient-like scavenging behavior of ^{10}Be (Kusakabe et al., 1990), a net export of ^{10}Be from the Atlantic to the Pacific, or from higher levels of ^{10}Be scavenging removal in the narrower and more particle-rich Atlantic basin, relative to the wide Pacific (e.g., Kaste and Baskaran, 2012), remains an open question. Previous work has highlighted the utility of sedimentary ^{10}Be to constrain past changes in water mass mixing (e.g., Jeromson et al., 2024; Frank et al., 2002; Sellén et al., 2009), though these efforts have not been employed in the open ocean on a large scale, in part because of complications associated with coeval changes in particle scavenging.

An improved understanding of the relative importance of water mass and particle scavenging in controlling ^{10}Be variability in marine sediments would enable refined utilization of meteoric ^{10}Be to reconstruct past environmental variability. For example, if the impact of changing ocean circulation and particle scavenging on temporal variations in sedimentary records of ^{10}Be can be credibly untangled and past variations in the ^{10}Be production rate can be independently constrained, then ^{10}Be could be used to investigate past changes in depositional environments and possibly basin-scale ocean circulation, analogous to the application of the shorter-lived protactinium-231 (^{231}Pa; ~33 kyr half-life) and thorium-230 (^{230}Th; ~75 kyr half-life) isotope systems (e.g, McManus et al., 2004; Waelbroeck et al., 2018; Jonkers et al., 2015). While their faster radioactive decay limits paleoceanographic applications of ^{231}Pa and ^{230}Th to the past ~150 kyr and ~500 kyr, respectively, ^{10}Be could be paired with stable extraterrestrial helium-3 (McGee and Mukhopadhyay, 2013) to investigate paleoceanographic variability throughout the complete Pleistocene, Pliocene, and even into the late Miocene.

Here we examine the oceanographic factors driving spatial and temporal variability in ^{10}Be fluxes to the seafloor across multiple depositional environments and time periods using a global compilation of marine sedimentary excess ^{230}Th ($^{230}Th_{XS}$)-normalized ^{10}Be flux data. Our compilation comprises data from 141 sediment core locations and 37 down-core time series, including 6 new time series records generated in the frame of this study. We focus specifically on measurements of $^{230}Th_{XS}$-normalized ^{10}Be fluxes, rather than ^{10}Be/^{9}Be ratios, to quantify variations in particulate scavenging of Be across different depositional environments and to isolate changes in ^{10}Be systematics from background changes in lithogenic ^{9}Be supply. With our analysis, we aim to improve characterization of the first-order processes governing ^{10}Be fluxes to the seafloor and thus refine application and interpretation of ^{10}Be as a paleoceanographic proxy throughout the late Neogene.

2. Sampling and methods

2.1. New Th-Be data

2.1.1. Study regions for new Th-Be records

We combine new ^{10}Be data with new and previously published U-Th isotope records for 6 sediment cores from the North Pacific, the equatorial Pacific, and the North Atlantic (Fig. 1). All Th-Be data presented here represent isotope measurements performed on co-located sediment samples from the same sediment cores (Supplementary Tables 1 and 2).

SeaVOICE Cores AT26-19-09PC (44.887°N, 130.637°W, 2678 m water depth) and AT26-19-12PC (44.897°N, 130.504°W, 2689 m water depth) were retrieved from the western flank of the Juan de Fuca Ridge in the northeast Pacific. Core descriptions, age models, thorium isotope, opal and calcium carbonate ($CaCO_3$) data are available in Costa et al. (2016), Costa and McManus (2017), Costa et al. (2018), and Costa (2018). Although hydrothermal scavenging can complicate interpretation of $^{230}Th_{XS}$ concentrations in near-ridge sediments, recent

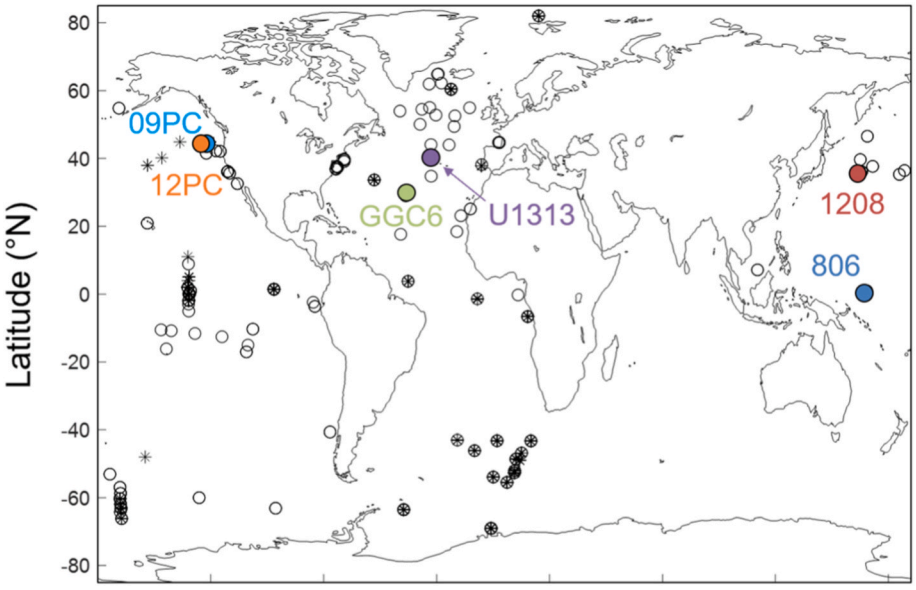

Fig. 1. Locations of compiled Be-Th sediment data (this study and references in Supplemental Table 1). Open circles indicate core top samples, filled circles indicate time series records. We present new records for ODP Site 806, ODP Site 1208, IODP Site U1313, and sediment cores AT26-19-09 PC, AT26-19-12 PC, and KN207-2-GGC6 (highlighted).

$^{3}He_{ET}$-analyses suggest insignificant hydrothermal influence on $^{230}Th_{XS}$-accumulation rates in any 09 PC sediments or in 12 PC sediments deposited after ~300 ka (Middleton et al., 2020). We present new ^{10}Be data for over 40 samples between these two sites, spanning the last 440 kyr.

ODP Site 1208A (36.127°N, 158.201°E, 3346 m water depth) was retrieved from the Shatsky Rise in the northwest Pacific during Leg 198 of the Ocean Drilling Program (Bralower et al., 2002). The age model, thorium isotope, opal, and $CaCO_3$ data for the Holocene/LGM interval evaluated in this study are available in Kinsley et al. (2022). We present new ^{10}Be data for 10 samples at this site spanning the last 50 kyr.

ODP Site 806A (0.318°N, 159.357°E, 2520 m water depth) was retrieved from the Ontong Java Plateau in the western equatorial Pacific during Leg 130 of the Ocean Drilling Program (Kroenke et al., 1991a). We develop a high-resolution age model for the targeted interval of Site 806A based on stratigraphic alignment to the well-dated record of Site 806B (Lea et al., 2000) using the shipboard magnetitic susceptibility data for both holes (Kroenke et al., 1991b; Supplementary Fig. 1). Our 806A age model is consistent with the 806A age interpretation of Wara et al. (2005). We present new U-Th and ^{10}Be data for 14 samples at this site spanning the last 150 kyr.

KN207-2-GGC6 (29.21°N, 43.23°W, 3018 m water depth) was retrieved from the axial valley of the Broken Spur segment of the Mid-Atlantic Ridge. The age model and thorium isotope data for this site are presented in Middleton et al. (2018). Although this core was recovered in proximity to the Broken Spur hydrothermal field, iron and copper measurements suggest little to no hydrothermal deposition at this location over the past 70 kyr (Middleton et al., 2020). We present new ^{10}Be data for 14 samples at this site spanning the last 70 kyr.

IODP Site U1313 (41.000°N, 32.957°W, 3426 m water depth) was retrieved from the western flank of the Mid-Atlantic Ridge during Expedition 306 of the International Ocean Drilling Program and constitutes a reoccupation of DSDP Site 607 (Channell et al., 2006). The age model and previously published thorium isotope data are from Smith et al. (2013), Naafs et al. (2013), and Zhou et al. (2025). We present additional U-Th data and new ^{10}Be data for 10 samples at this site spanning the last 140 kyr.

2.1.2. Beryllium isotope measurements

Beryllium sample preparation for GGC6, 12PC, 09PC, 1208A, 806A, and U1313 was performed at the Lamont-Doherty Earth Observatory (LDEO). For each analysis, 100 mg aliquots of dry bulk sediment were spiked with 200 mg of 1000 ppm ^{9}Be Spex CertiPrep carrier solution and digested in concentrated perchloric acid, nitric acid (HNO_3), and hydrofluoric acid. A hydroxide precipitation was performed to remove soluble metals (Na, K, Ca) prior to column chemistry. The sample solutions were adjusted to pH ~9 using ammonium hydroxide (NH_4OH) and the insoluble hydroxide precipitate, containing the beryllium fraction as well as other hydroxides (Al, Ti, Fe, Mn), was rinsed and redissolved in concentrated hydrochloric acid (HCl).

Excess hydrochloric acid was burned off on a hotplate and samples were taken up in 3 ml of 9M HCl prior to chromatographic separation on 5 ml AG1-x8 100-200 mesh BioRad resin anion exchange columns, to remove Fe and Mn. The sample fraction was eluted from the anion exchange resin with 14 ml of 9M HCl and dried down overnight at 100C in the presence of 1 ml of 0.5M sulfuric acid, followed by two additional evaporations with miliQ water containing trace sulfuric acid and hydrogen peroxide. The final sample residue was taken up in 3 ml of miliQ water with trace sulfuric acid and hydrogen peroxide and loaded onto 4 ml DOWEX-50 x8 200-400 cation exchange resin to isolate Be from Al and Ti.

Sample beryllium was eluted from the cation exchange resin using 20 ml of 1.2M HCl and dried down at 150°C in the presence of 5 drops of concentrated HNO_3. The isolated sample beryllium was further purified twice via beryllium hydroxide precipitation at pH 9 using ~200 μl of NH_4OH and redissolution in 100 μl of 8M HNO_3, followed by rinsing with deionized water at pH 8. The residual beryllium hydroxide precipitates were then transferred to quartz crucibles for combustion at 830°C and packed into stainless steel cathodes with ~9 mg niobium powder (99.99% metals basis) for analysis. Beryllium isotope analyses were performed on the accelerator mass spectrometer (AMS) at Lawrence-Livermore National Laboratory. The 1σ analytical uncertainty in reported ^{10}Be concentrations is less than 1% for all cores with the exception of Site 806A, where it varied from 1 to 2%.

2.1.3. Uranium-thorium isotope measurements

Thorium isotope measurements and $^{230}Th_{XS}$-derived mass accumulation rates for Site 806A and U1313 were determined following the methods of Costa and McManus (2017) and Costa et al. (2020). In brief, 100 mg sediment aliquots were spiked with ^{229}Th and ^{236}U, digested in

concentrated perchloric, nitric, and hydrofluoric acids, chromatographically separated, and measured on an inductively coupled plasma mass spectrometer at the Lamont-Doherty Earth Observatory following the procedure of Fleisher and Anderson (2003). Concentrations of $^{230}Th_{XS}$ and $^{230}Th_{XS}$-derived mass accumulation rates, hereby referred to as bulk sediment fluxes, were calculated for each sample following Costa et al. (2020), using the basin-specific lithogenic $^{238}U/^{232}Th$ activity ratios of Henderson and Anderson (2003). All $^{230}Th_{XS}$-derived fluxes presented here were calculated from initial, decay-corrected, $^{230}Th_{XS}$ concentrations (also known as $^{230}Th_{XS,0}$) based on the published age information for each sample. Throughout this study, we express the initial, decay-corrected, excess ^{230}Th concentration as $^{230}Th_{XS}$ for simplicity, unless otherwise noted.

The $^{230}Th_{XS}$-derived ^{10}Be and ^{232}Th fluxes were then computed by multiplying the $^{230}Th_{XS}$-derived bulk sediment flux of each sample by its ^{10}Be concentration and ^{232}Th concentration, respectively. The long-term analytical uncertainties of U-series measurements were constrained via repeat analysis of the VIMS (SeaVOICE Internal Mega Standard; Costa and McManus, 2017) and NAIMS (North Atlantic Internal Mega Standard; Costa et al., 2024; Zhou et al., 2025) homogenized sediment mixtures, which indicate 1σ analytical uncertainties of 1-3% for the ^{238}U, ^{230}Th, and ^{232}Th concentration data.

2.2. Global compilation of sedimentary ^{10}Be fluxes

We examine the new $^{230}Th_{XS}$-normalized ^{10}Be flux data of this work within the context of a global compilation of $^{230}Th_{XS}$-normalized ^{10}Be data from 141 sedimentary records (Fig. 1). While $^{10}Be/^{9}Be$ data is valuable in understanding Be isotope systematics and their implications for modern and paleoceanography (e.g., Savranskaia et al., 2021), only sediment Be records with complementary thorium isotope data were included in this compilation to allow direct flux comparison across diverse depositional environments and to account for potential complications associated with lateral sediment redistribution (e.g., Costa et al., 2020).

Sediment ^{10}Be, Th isotope, and sediment composition data were retrieved from the National Oceanic and Atmospheric Administration (NOAA) National Centers for Environmental Information (NCEI) Paleoclimatology, the Biological and Chemical Oceanography Data Management Office (BCO-DMO), and the PANGAEA Data Publisher for Earth and Environmental Sciences online databases, as well as tables and supplementary data sets available in the existing literature (Supplementary Tables 1 and 2; Bernsdorff, 2008; Chase et al., 2003a; Christl et al., 2010; Costa and McManus, 2017; Costa et al., 2018; Eisenhauer et al., 1994; Frank et al., 1994; Frank et al., 1995; Frank et al., 1996; Frank et al., 1997; Frank et al., 2000; Geibert et al., 2021; Kinsley et al., 2022; Kumar et al., 1995; Lao et al., 1992; Lippold et al., 2016; Marcantonio et al., 1996; Marcantonio et al., 2001; Ménabréaz et al., 2011; Middleton et al., 2018; Middleton et al., 2020; Pavia et al., 2024; Rutsch et al., 1995; Anderson et al., 1994). The global compilation also includes previously unpublished ^{10}Be data generated by the LDEO group in sediment core samples from JGOFS cruise TT013 to the central equatorial Pacific (Supplementary Tables 1 and 2) and assorted North Atlantic core tops (Supplementary Tables 1 and 2). Core descriptions, U-Th isotope data, and sediment composition data for these samples are available in Berelson et al. (1997), Marcantonio et al. (1995), Murray et al., 1995, Marcantonio et al. (2001), Murray et al., 2000, Anderson et al. (2006, 2008), and Leal et al. (2025). The ^{10}Be data for these samples were generated following the methods of Lao et al. (1993).

Samples for which ^{10}Be concentrations were measured using sediment leachate methods (e.g., Henken-Mellies et al., 1990), in contrast to bulk sediment material (e.g., Lao et al., 1993; Anderson et al., 1990), are flagged within the compilation tables. Where distinct concentration data and reasonable constraints on lithogenic $^{238}U/^{232}Th$ ratios are available, all $^{230}Th_{XS}$ concentrations and fluxes, as well as ^{10}Be decay corrections, were recalculated according to the values and methods listed in Costa et al. (2020), Chmeleff et al. (2010), and Korschinek et al. (2010) to maximize consistency in proxy utilization across multiple studies and sedimentary records. Where available, sedimentary opal, $CaCO_3$, and ^{232}Th data, used as a lithogenic proxy (e.g., Kienast et al., 2016), were also compiled to examine the effects of variations in particle composition and flux on scavenging intensity and sedimentary ^{10}Be fluxes. Of the 141 total records in the compilation, all include ^{232}Th data, 50 include complementary opal data, and 25 include $CaCO_3$ data.

Sedimentary records recovered from locations in complex scavenging environments, such as those with significant levels of hydrothermal input, were flagged and excluded from the global compilation as these settings can bias the $^{230}Th_{XS}$ constant flux proxy system (Costa et al., 2020; Middleton et al., 2020). Given increased uncertainties in the utilization of $^{230}Th_{XS}$ within the GEOTRACES GP16 core top samples of the South Pacific Gyre (Pavia et al., 2024), we have substituted extraterrestrial helium-3 ($^{3}He_{ET}$) normalized flux data for the $^{230}Th_{XS}$ data of these samples. Additional records or samples within the compiled data set that were identified within the literature as not representative of typical marine sedimentary conditions, such as those from the glauconite rich Core PSBC-133 from the California Margin (Lao et al., 1992) or Arctic record PS1533-3 (Geibert et al., 2021) were also excluded from compilation data analysis and interpretation.

While our compilation of $^{230}Th_{XS}$-normalized sedimentary ^{10}Be flux records includes data spanning the high and low latitude regions of the Atlantic and Pacific Oceans, we note that it noticeably lacks sample coverage in the Indian Ocean (Fig. 1). We encourage the generation of more $^{230}Th_{XS}$ -^{10}Be data in the Indian Ocean basin in order to determine whether the oceanographic patterns impacting sedimentary ^{10}Be fluxes observed in the Pacific and Atlantic basins are globally applicable, or whether Be systematics in the Indian Ocean are sensitive to local oceanographic conditions.

2.3. Paleomagnetic corrections of ^{10}Be production

As a cosmogenic nuclide, variations in the intensity of Earth's magnetic field will change the atmospheric production rate of ^{10}Be over time (Lal and Peters, 1967). Unless otherwise specified, we correct downcore ^{10}Be fluxes for paleomagnetic variations by dividing by the paleo-^{10}Be production rate for each age and thus provide flux variations relative to the late Holocene average (2-6 ka). Paleo-^{10}Be production rates are computed using the production rate equations of Wagner et al. (2000), the sediment core age models, and the PISO-1500 paleomagnetic intensity reconstruction (Channell et al., 2009). The PISO-1500 stack is preferred for this analysis due to its simultaneous alignment with benthic foraminiferal oxygen isotope data, from which many sediment core age models have been generated, and its sensitivity to high frequency variability in relative paleo intensity (Channell et al., 2009). We additionally examine the relationship between downcore ^{10}Be fluxes and paleo-^{10}Be production rates computed using the SINT-2000 paleomagnetic intensity reconstructions (Valet et al., 2005) as a sensitivity test to the choice of the paleomagnetic record used to produce corrected ^{10}Be flux timeseries.

2.4. Basin-specific analyses

In order to evaluate basin-specific relationships between ^{10}Be fluxes and other oceanographic factors, sediment sample locations were assigned to either the Atlantic, Southern Ocean, or Pacific basins based on their pre-industrial bottom water radiocarbon values ($\Delta^{14}C$). Pre-industrial bottom water radiocarbon values were interpolated to each sample location based on OCIM2-48L (Holzer et al., 2021). Sample locations with $\Delta^{14}C$ values greater than −125‰ were assigned to the Atlantic, those with $\Delta^{14}C$ values between −125 and −175‰ were assigned to the Southern Ocean, and those with $\Delta^{14}C$ values below −175‰ were assigned to the Pacific basin.

3. Results

3.1. New ^{10}Be flux time series

Our new $^{230}Th_{XS}$-normalized sedimentary ^{10}Be flux records illustrate the range and temporal variability of seafloor ^{10}Be fluxes across multiple depositional environments and ocean basins, including the North Atlantic (IODP Site U1313), the subtropical North Atlantic gyre (KN207-2-GGC6), the western equatorial Pacific (ODP Site 806), and the western (ODP Site 1208) and eastern (AT26-19-09PC and AT26-19-12PC) North Pacific margins (Fig. 2). Comparison of these records with paleomagnetic intensity data highlights the magnitude of climate-driven variability in seafloor ^{10}Be fluxes relative to changes in atmospheric ^{10}Be production rates associated with magnetic field intensity (Fig. 2; Channell et al., 2009; Wagner et al., 2000). For example, the non-production-rate-corrected sedimentary ^{10}Be fluxes during the Last Glacial Maximum (LGM; ~18-24 ka) were generally 2-4 times higher than the minimum Holocene ^{10}Be fluxes (between 0 and 10 ka), whereas the PISO-1500 geomagnetic intensity reconstruction suggests that atmospheric ^{10}Be production was less than ~10% higher during the LGM (Fig. 2).

Notably, there is no significant correlation between the uncorrected seafloor ^{10}Be fluxes and the relative atmospheric production rate calculated for each sample age (via Wagner et al., 2000; Channell et al., 2009, Fig. 2). This observation demonstrates the impact of oceanographic and climatic effects on sedimentary ^{10}Be fluxes relative to estimated changes in the atmospheric ^{10}Be production rate over time. Consequently, improved constraints on the oceanographic variables driving variations in seafloor ^{10}Be fluxes are essential to understand long term changes in sedimentary ^{10}Be records.

Strong correlations between sedimentary ^{10}Be fluxes and lithogenic ^{232}Th fluxes across basins ($R^2 = 0.66$ for the aggregated data set) suggest that variations in lithogenic particle scavenging are a primary driver of the variability in ^{10}Be fluxes observed at these sites (Fig. 2). Beyond the general linear relationship between lithogenic and ^{10}Be fluxes, there also appears to be an ocean basin-effect on seafloor ^{10}Be fluxes, with Pacific sites (806, 1208, 09PC and 12PC) exhibiting higher ^{10}Be fluxes for a given lithogenic ^{232}Th flux than the Atlantic Sites (U1313 and GGC6; Fig. 2i). When the time series records are grouped by ocean basin, the observed correlation between ^{10}Be and lithogenic ^{232}Th fluxes increases (Pacific $R^2 = 0.79$, Atlantic $R^2 = 0.93$).

Although the Atlantic sites exhibit a weak correlation between sedimentary ^{10}Be flux and bulk sediment fluxes ($R^2 = 0.36$), no meaningful relationship is observed in the Pacific or aggregate data (Fig. 2). Given that bulk sediment accumulation rates at many of these sites are dominated by calcium carbonate (e.g., Costa et al., 2016; Middleton et al., 2018; Kroenke et al., 1991a; Channell et al., 2006), these observations may reflect the overall weaker influence of calcium carbonate on ^{10}Be particle scavenging (e.g., Chase et al., 2002) or a disconnect between carbonate deposition and ^{10}Be accumulation possibly driven by variable $CaCO_3$ dissolution and preservation. Alternatively, the lack of correlations between ^{10}Be fluxes and bulk sediment fluxes may result from variable opal deposition, which efficiently increases ^{10}Be fluxes without adding significantly to the bulk sediment flux, as is observed at Site 1208 (Fig. 2). The impacts of opal are difficult to fully assess within the new time series records, as opal data are only available for ODP Site 1208 (Kinsley et al., 2022) and SeaVOICE core AT26-19-09PC (Costa et al., 2018).

We now examine the relationships observed in our new $^{230}Th_{XS}$-^{10}Be records within the context of our global $^{230}Th_{XS}$-^{10}Be compilation in

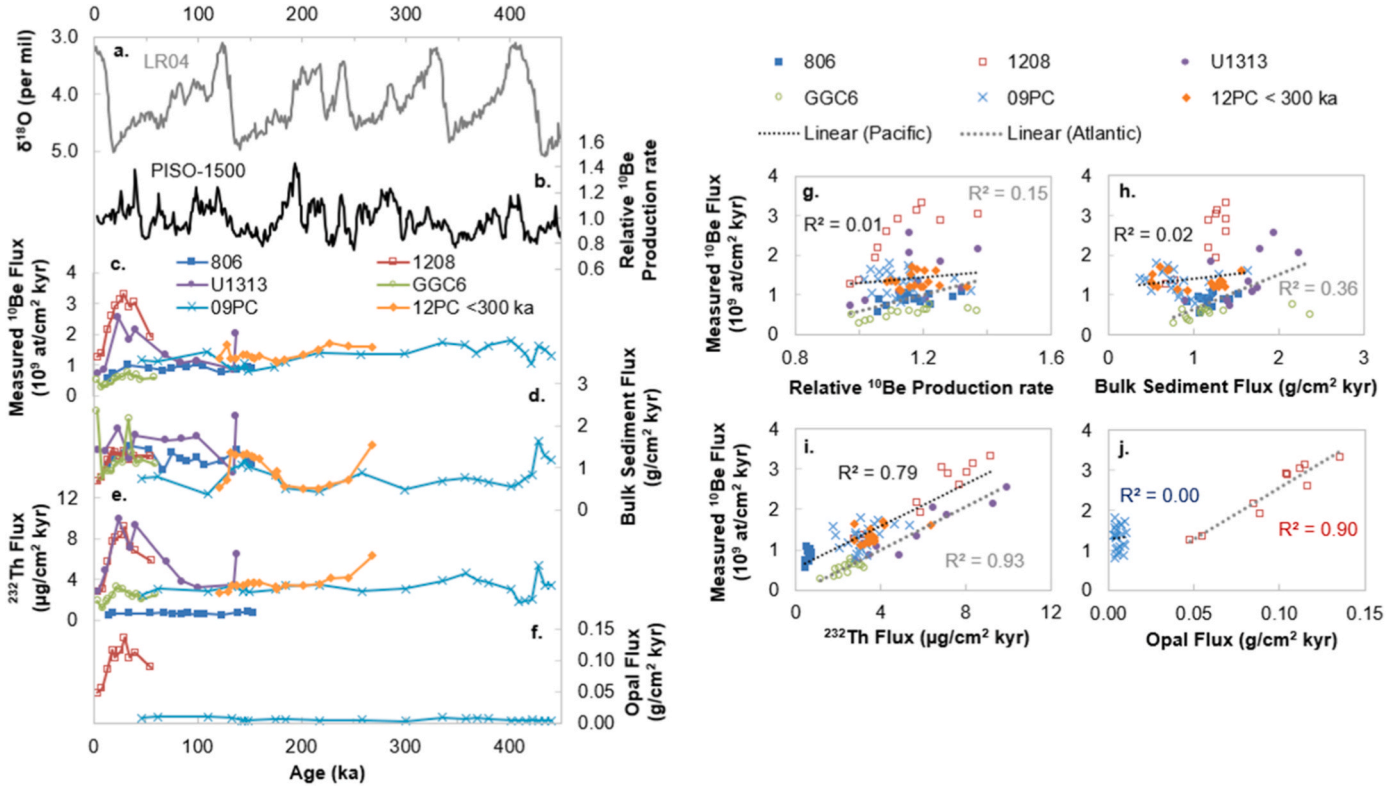

Fig. 2. New Th-Be time-series and correlation data for ODP Site 806, ODP Site 1208, IODP Site U1313, and cores AT26-19-09PC, AT26-19-12PC, and KN207-2-GGC6. (a) the LR04 benthic foraminifera oxygen isotope ($\delta^{18}O$) stack over the past 450 ka for climatic reference (Lisiecki and Raymo, 2005); (b) variations in the atmospheric ^{10}Be production rate relative to the late Holocene, calculated from PISO-1500 (Wagner et al., 2000; Channell et al., 2009); (c) ^{10}Be flux records; (d) bulk sediment flux records; (e) ^{232}Th flux records; (f) opal flux records, where available for ODP Site 1208 and AT26-19-09PC (Costa et al., 2018; Kinsley et al., 2022); (g-j) ^{10}Be flux data versus (g) the coincident relative ^{10}Be production rate (as in (b)); (h) bulk sediment flux; (i) ^{232}Th flux; (j) opal flux data, where available. All fluxes are calculated using $^{230}Th_{XS}$-normalization. The ^{10}Be flux records in this figure have not been corrected for past changes in atmospheric production rate.

order to determine whether the patterns observed here (e.g., the strong correlation between lithogenic fluxes and ^{10}Be fluxes and higher ^{10}Be fluxes in the Pacific than the Atlantic) are also present on a global scale, when data from the Southern Hemisphere and additional regions with high opal fluxes are included as well. We first consider the global core top/Holocene data set before examining temporal variability within the compiled time series data.

3.2. Global core-top/Holocene data set

Globally, $^{230}Th_{XS}$-normalized ^{10}Be fluxes in compiled core-top sediment samples (or the youngest measured sample <10 ka if core top data is unavailable) show a range of two orders of magnitude, from 0.06 to 4.9 × 10^9 atoms/cm^2 kyr (Fig. 3). The highest seafloor ^{10}Be fluxes occur in the high latitude North Atlantic (>50°N), the Southern Ocean, and along some, but not all, continental margins. The lowest seafloor ^{10}Be fluxes are found in the subtropical North Atlantic and the tropical Pacific.

3.2.1. Marine scavenging factors

We calculated a marine scavenging factor for each core-top sample by dividing its ^{10}Be flux by the global meteoric ^{10}Be production rate, such that values greater than one indicate excess seafloor ^{10}Be fluxes and values below one indicate depleted seafloor ^{10}Be fluxes (Fig. 4a). For these calculations, a modern global ^{10}Be production rate value of 1.09 × 10^9 atoms/cm^2 kyr (Heikkila and von Blanckenburg, 2015) was applied, which is well within the range of previous estimates (Masarik and Beer, 2009). We use the global average ^{10}Be production rate, rather than the spatially heterogenous sea surface ^{10}Be fluxes (e.g., Heikkila and von Blanckenburg, 2015), based on the assumption that the 200-1000 year residence time of ^{10}Be in seawater enables thorough mixing (Anderson et al., 1990; Ku et al., 1990; Kaste and Baskaran, 2012). The map of marine scavenging factors obtained from the core-top data exhibits spatial patterns similar to the map of absolute ^{10}Be fluxes and suggests that the excess ^{10}Be fluxes observed in the particle-rich, high-scavenging regions of the high latitude North Atlantic, the Southern Ocean, and along continental margins may be balanced by ^{10}Be depletion, and thus lower ^{10}Be fluxes, in the abyssal plains of the subtropical gyres (Fig. 4a).

Interestingly, core-top sediments from the Northwest African margin exhibit depleted marine scavenging factors (values less than one), despite their proximity to the continent and the high particle fluxes observed at these sites (Figs. 3 and 4). The relative ^{10}Be depletion along the Northwest African margin contrasts with other continental margin upwelling areas, such as coastal California and the Peruvian margin, where the marine scavenging factors suggest ^{10}Be fluxes exceeding 1.5x the global production rate or higher (Fig. 4). The relatively low ^{10}Be fluxes observed in Northwest African margin sediments, compared to other continental margin areas, is spatially consistent with the relative low sea surface ^{10}Be depositional fluxes predicted over this region by climate models (Fig. 4b; Heikkila and von Blanckenburg, 2015). Although ocean mixing is thought to homogenize spatial variability in atmospheric ^{10}Be deposition to the sea surface, the Northwest African margin, with its very low precipitation rates and high lithogenic fluxes, may represent a unique setting where this presumed homogenization may not be occurring.

From a basin-specific perspective, while the Atlantic core-top data exhibit a range of marine scavenging factors (both above and below 1) consistent with variable ^{10}Be excesses and depletions, dependent on the local depositional settings, nearly every Southern Ocean core-top examined exhibits a marine scavenging factor indicative of excess ^{10}Be deposition (Fig. 4). This pattern suggests that, despite several regions of excess ^{10}Be deposition within the Atlantic basin, there is net export of seawater ^{10}Be from the Atlantic into the Southern Ocean that results in Southern Ocean sedimentary ^{10}Be fluxes consistently higher than the global production rate. Like in the Atlantic, the Pacific core-top data exhibit a range of marine scavenging factors indicative of variable ^{10}Be excesses and depletions. Whether there is also a net export of seawater ^{10}Be from the Pacific into the Southern Ocean cannot be determined with the available data, as many Pacific regions that are likely to exhibit significant ^{10}Be scavenging, such as equatorial upwelling regions and the East Pacific Rise, are not representatively sampled in this compilation.

3.2.2. Impact of scavenging particle composition

The observed global pattern of core-top ^{10}Be fluxes likely reflects the influence of marine particle scavenging on ^{10}Be systematics and exhibits a moderate correlation with $^{230}Th_{XS}$-normalized bulk sediment fluxes (R^2 = 0.39, n = 212) at the same locations (Table 1; Fig. 3d). Core-top ^{10}Be fluxes exhibit similar linear correlations (Fig. 3) with lithogenic ^{232}Th fluxes (R^2 = 0.31, n = 212) and opal fluxes (R^2 = 0.44, n = 78 due to smaller available data set), although the global opal data are better explained by a logarithmic relationship (R^2 = 0.60, n = 78). Where data is available (n = 63), the relationship between global core-top ^{10}Be fluxes and $CaCO_3$ fluxes is negligible or non-linear, with a wide range of ^{10}Be fluxes associated with very low $CaCO_3$ flux values. This apparent non-linear negative relationship between ^{10}Be and $CaCO_3$ fluxes on a global scale may reflect a weaker, but non-zero, scavenging influence of $CaCO_3$ on ^{10}Be, relative to opal and lithogenic particles. These correlations are based on the complete global core-top sample set, including both leached and bulk-processed samples.

Some of the variability in the core-top data set can be reduced by removing six outlier samples from three hemipelagic cores from the global analysis. These cores are vt19-28 and vt19-29 from the Ecuador Margin (Lao et al., 1992) and GeoB1008-3 from the Congo Margin (Rutsch et al., 1995; Frank et al., 1996). Given the proximity of each of these cores to a nearby river mouth, the relatively high ^{10}Be fluxes observed in these samples may result from additional ^{10}Be inputs to these locations, in excess of the global average ^{10}Be production rate, due to river runoff and particulate scavenging of ^{10}Be originally deposited on land (Deng et al., 2025). When these six samples are removed from the global analysis, we observe a modest increase in correlations between core-top ^{10}Be fluxes and bulk sediment fluxes (R^2 = 0.41, n = 206), lithogenic ^{232}Th fluxes (R^2 = 0.33, n = 206), and opal fluxes (R^2 = 0.45, n = 75). This sample elimination does not impact the $CaCO_3$ data set. Based on this observation, all following results in this study are calculated based on the exclusion of samples from these hemipelagic sites.

Notably, bulk sediment fluxes are not correlated with ^{10}Be fluxes within the data set that only includes samples with available opal data (n = 75; *Opal Only* data set in Table 1). The *Opal Only* data set is heavily weighted towards records from regions with high opal fluxes, such as upwelling regions and the Southern Ocean (Supplementary Table 2). This result suggests that model estimates of seafloor ^{10}Be fluxes based solely on bulk sediment flux are unlikely to appropriately capture ^{10}Be flux variability within these regions of high opal productivity. When samples with the highest opal fluxes relative to bulk sediment fluxes, indicated by high opal concentrations, are progressively removed from the global core-top data set, the correlations between ^{10}Be fluxes and bulk sediment fluxes, as well as lithogenic sediment fluxes, begin to improve (Supplementary Fig. S2). For the *Some Opal* core-top/Holocene data set (n = 181), which includes all samples with less than 40 wt% opal, ^{10}Be fluxes exhibit higher correlations with bulk sediment fluxes (R^2 = 0.51), and with lithogenic ^{232}Th fluxes (R^2 = 0.50; Table 1). Thus, although opal deposition uniquely impacts ^{10}Be fluxes to the seafloor, ^{10}Be scavenging via opal particles does not appear to dominate the ^{10}Be flux signal except in highly opal-rich sediments (e.g., greater than 40 wt % opal).

3.2.3. Impact of leaching on measured ^{10}Be fluxes

The ^{10}Be fluxes measured in leached versus bulk-processed samples may be expected to differ if the ^{10}Be input from background sediment particles, such as lithogenic material, were high relative to the leachable meteoric ^{10}Be input scavenged from seawater, as is the case for ^{9}Be.

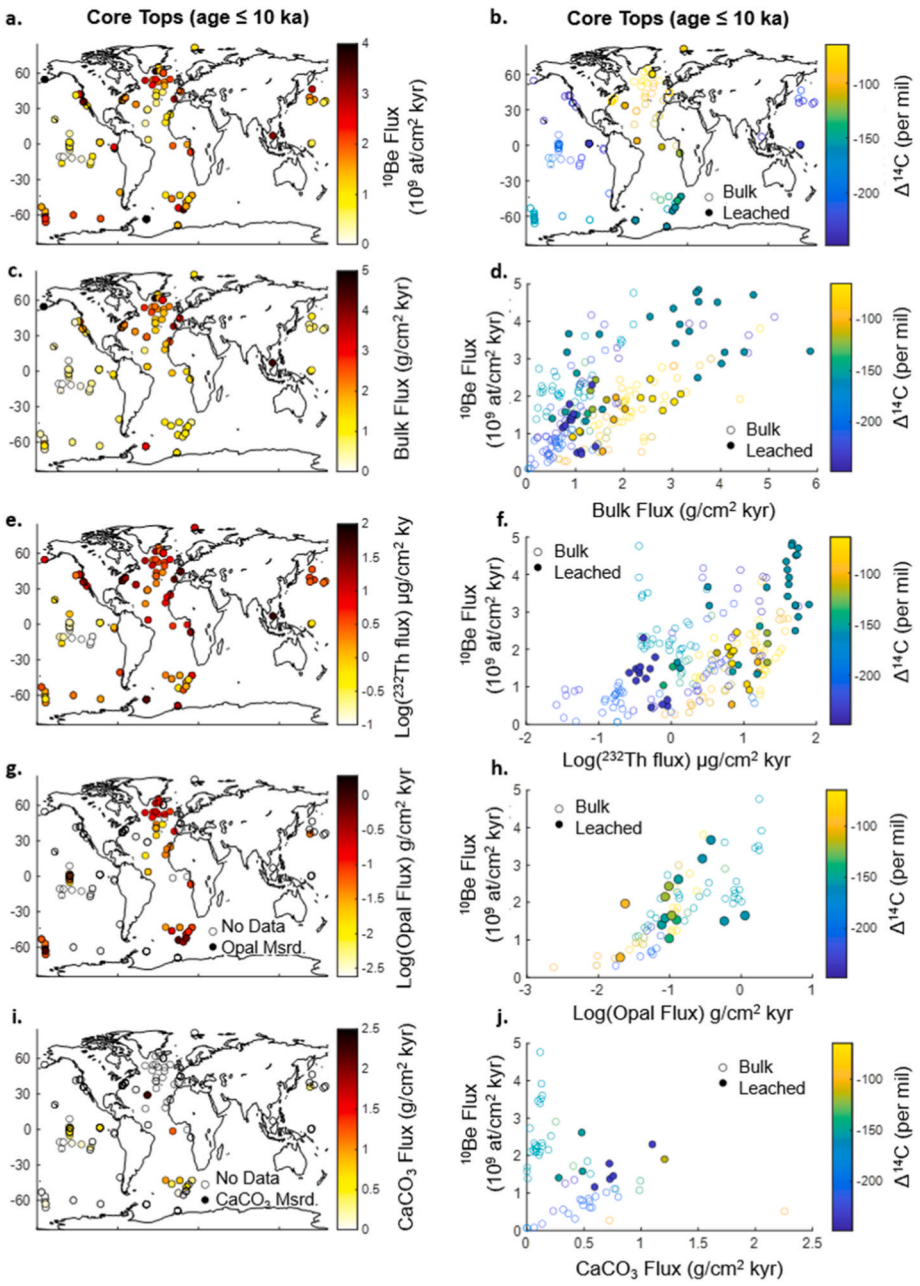

Fig. 3. Core-top/Holocene compilation parameter maps and correlation plots. (a) $^{230}Th_{XS}$-normalized ^{10}Be fluxes; (b) pre-industrial bottom water Δ^{14}C values at each core location for spatial reference (Holzer et al., 2021); (c) Bulk sediment fluxes and (d) correlation with ^{10}Be fluxes; (e) ^{232}Th fluxes and (f) correlation with ^{10}Be fluxes; (g) opal fluxes and (h) correlation with ^{10}Be fluxes; (i) $CaCO_3$ fluxes and (j) correlation with ^{10}Be fluxes. In (b,d,f,h, and j), open circles indicate ^{10}Be flux values derived from bulk sediment analysis, while filled circles indicate ^{10}Be flux values derived from leached sediment analysis. In (g and i), filled circles indicate samples with available opal or $CaCO_3$ flux data, while open circles indicate samples for which opal or $CaCO_3$ data is not available. Opal and ^{232}Th fluxes are plotted on a log scale for visual clarity. All fluxes are calculated using $^{230}Th_{XS}$-normalization, with the exception of GEOTRACES GP16 core top samples from the equatorial Pacific, which are calculated using $^{3}He_{ET}$ -normalization (Pavia et al., 2024).

Within the global core-top data set, reported ^{10}Be concentrations range from 0.2 to 11.5 × 10^9 atoms/g (Supplementary Table 2). In comparison, ^{10}Be concentrations measured in loess and aeolian dust, the likeliest sources of lithogenic ^{10}Be to the abyssal seafloor, are typically on the order of 0.1-5 x 10^8 atoms/g (Graham et al., 2003; Gu et al., 1996; Willenbring and von Blanckenburg, 2010b). Importantly, these dust studies note that the reported ^{10}Be concentrations may include both original ^{10}Be produced by cosmic radiation within the mineral lattice of the dust itself (*in situ* ^{10}Be), as well as meteoric ^{10}Be already scavenged and retained onto the sample particles. The fate of the meteoric ^{10}Be on such particles through atmospheric transport processes and prolonged exposure to seawater remains unclear. A more appropriate upper limit for *in situ* lithogenic ^{10}Be concentrations may be better approximated by bedrock samples from the Antarctic Dry Valleys, where high polar *in situ* ^{10}Be production rates and multi-million-year exposure ages support bedrock ^{10}Be concentrations on the order of 0.1-5 x 10^7 atoms/g (e.g., Balco and Shuster, 2009; Balter-Kennedy et al., 2023). Hence, the true concentration of lithogenic ^{10}Be expected within the marine sediments of this study may reasonably be expected to be closer to the 1 × 10^7 atoms/g range or lower (Willenbring and von Blanckenburg, 2010b), orders of magnitude lower than total ^{10}Be concentrations observed within the marine sediment compilation.

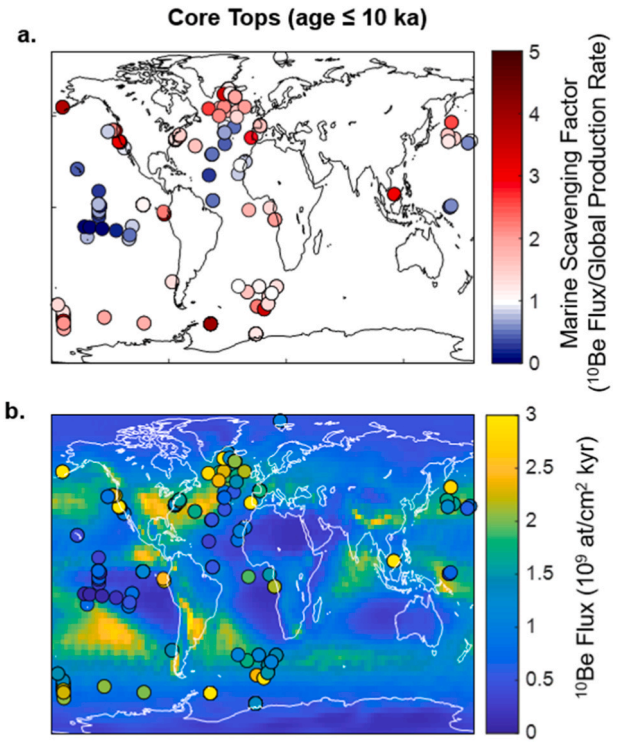

Fig. 4. Map of marine scavenging factors for the complete core-top/Holocene data set. (a) Marine scavenging factors were calculated for each sample by dividing its ^{10}Be flux by the global meteoric ^{10}Be production rate of 1.09×10^9 atoms/cm^2 kyr (Heikillia and von Blanckenburg, 2015). (b) Comparison map of sedimentary core-top/Holocene ^{10}Be fluxes with model estimates for ^{10}Be deposition rates to the sea and land surface (Heikillia and von Blanckenburg, 2015). The color axis in (b) is truncated to highlight regional variability in the deposition model estimates.

Consequently, we expect meteoric ^{10}Be to dominate the total ^{10}Be budget of marine sediments and thus do not expect a significant difference in ^{10}Be values derived from sample leaching versus bulk sediment processing. Our compilation analysis supports this conclusion as we do not observe a systematic difference in the ^{10}Be fluxes and apparent relationships with sediment particle fluxes between samples with ^{10}Be data determined from the leachate versus bulk sediment analytical procedures (Fig. 3). Quantitative assessment of this observation, however, is difficult due to the environmental variability among samples processed via leaching versus bulk sediment processing. For example, leached samples exhibit higher correlations between ^{10}Be fluxes and bulk sediment fluxes ($R^2 = 0.46$, n = 56) and lithogenic ^{232}Th fluxes ($R^2 = 0.59$, n = 56) than the bulk-processed samples ($R^2 = 0.31$ and the not meaningful $R^2 = 0.11$ for bulk sediment fluxes and ^{232}Th fluxes, respectively, n = 156; Table 1). However, bulk-processed samples represent a larger data set and include samples with higher opal-fluxes than the leached sample set (Fig. 3). Moving forward, all data interpretations in this work will be based on the combined leached and bulk-processed sample sets, unless otherwise noted.

3.2.4. *Impact of other environmental parameters*

The correlations between core-top ^{10}Be fluxes and other sediment particle fluxes are higher when evaluated in samples from the same ocean basin (Fig. 3; Table 1), as observed in the new time series discussed above. For the Atlantic (n = 64), Southern Ocean (n = 64) and Pacific (n = 78) core-top data sets, correlations between ^{10}Be fluxes and bulk sediment fluxes yield R^2 values of 0.57, 0.45, and 0.65, respectively. The basin-specific correlations between ^{10}Be fluxes and lithogenic ^{232}Th fluxes are lower than those observed with bulk sediment fluxes, but generally slightly higher than the lithogenic correlation observed in the global analysis (R^2 = 0.34, 0.37, and 0.35 for the Atlantic, Southern Ocean, and Pacific, respectively).

Beyond the influence of particle flux, we also evaluate correlations between core-top ^{10}Be fluxes and water depth (Table 1; Fig. 5). Seawater ^{10}Be typically follows nutrient-like profiles within the water column and thus seawater ^{10}Be concentrations tend to increase with water depth (Fig. 5a; Deng et al., 2025; Kusakabe et al., 1990; Chase et al., 2003b). The nutrient-like profiles of seawater ^{10}Be suggest the release of some fraction of surface-scavenged ^{10}Be via the dissolution of a scavenging particle phase, such as particulate organic matter, in the deep ocean. Although previous work has detected a global correlation between sedimentary ^{10}Be/^{9}Be ratios and depth (Savranskaia et al., 2021), we do not observe any significant correlation between $^{230}Th_{XS}$-normalized ^{10}Be fluxes and water depth in the global core-top data set or within the basin-specific core top data sets (Fig. 5b; Table 1). However, the observed correlations between global core top/Holocene ^{10}Be fluxes and bulk sediment fluxes are generally higher throughout the global data set when ^{10}Be flux values are first divided by sediment core water depth (Table 2). For example, when samples with opal concentrations exceeding 40 wt% are excluded, the correlation between depth-normalized ^{10}Be fluxes and bulk sediment fluxes yield R^2 values of 0.62, 0.36, 0.63, and 0.83 for the global data set (n = 205), the Atlantic (n = 63), the Southern Ocean (n = 64), and the Pacific data sets (n = 78), respectively (Table 2). These correlations were calculated based on exclusion of one flyer with an unusually high ^{10}Be flux/depth value from Atlantic site EN179 BC5 from 384 m water depth. Notably, only the Atlantic basin exhibits weaker correlations between ^{10}Be fluxes and bulk sediment fluxes when sediment core water depth is accounted for. This apparent depth-dependence may reflect a global pattern of increasing sediment ^{10}Be concentrations with depth (Fig. 5c), as the comparison of ^{10}Be flux divided by depth versus bulk sediment flux is mathematically equivalent to the comparison of sediment ^{10}Be concentrations and water depth.

We additionally examine the relationship between ^{10}Be fluxes and water mass age, approximated by the pre-industrial bottom water radiocarbon value (Δ^{14}C) for each core top site adopted from Holzer et al. (2021), because deep water ^{10}Be concentrations generally increase along the thermohaline circulation pathway (Fig. 5d; Deng et al., 2025; Kusakabe et al., 1987; Kusakabe et al., 1990). To first order, the core-top data do not exhibit any meaningful global or strong basin-specific correlations between ^{10}Be fluxes and bottom water Δ^{14}C (Fig. 5e; Table 1). This observation persists when ^{10}Be fluxes are normalized to sediment core water depth, with the exception of the Atlantic data set (Table 2). The Atlantic core top data exhibit a significant correlation between depth-normalized ^{10}Be fluxes and bottom water Δ^{14}C with an R^2 of 0.44 (n = 63). Interestingly, depth-normalized ^{10}Be fluxes and depth-normalized sediment ^{10}Be concentrations in the Atlantic core top data set appear to decrease with increasing water mass age (Fig. 6), which is contrary to the general trend observed in seawater ^{10}Be concentrations (Fig. 5a). However, we caution against overinterpretation of this result because it may arise from a sampling bias, given that the majority of Atlantic core top samples with the youngest radiocarbon values ($\Delta^{14}C > -80‰$) are from much shallower depths (<2000 m) than the rest of the Atlantic data set. Over all, our analysis of ^{10}Be fluxes and water mass ages suggests that the basin-specific relationships observed between ^{10}Be fluxes and sediment particle fluxes are not linearly related to deep ocean circulation, but likely reflect a more complex relationship with depth and water mass geometry.

3.3. *Global time series data set*

Much of the spatial coverage of the global compilation comes from core top or time slice studies that do not extend past the Last Glacial Maximum (~20 ka; LGM). Beyond the LGM, the number of time series records available decreases with each glacial cycle, with about 20 records extending past 100 ka and only four records extending past 300 ka

Table 1
Pearson R^2 values for correlations between core-top/Holocene (0-10 ka) sediment ^{10}Be fluxes and assorted environmental parameters.

	All Core Tops	Flyers Removed	Leached Samples	Bulk Samples	Atlantic[e] Core Tops	S. Ocean[e] Core Tops	Pacific[e] Core Tops
				^{10}Be Fluxes			
All Data (n)	*212*	*206*	*56*	*156*	*64*	*64*	*78*
Bulk flux	0.39*	0.41*	0.46*	0.31*	0.57*	0.45*	0.65*
^{232}Th flux	0.31*	0.33*	0.59*	0.11	0.34*	0.37*	0.35*
$\Delta^{14}C$[a]	-	-	-	-	0.13	0.11	0.26*
Depth	-	-	-	-	-	0.07	-
$CaCO_3$ Reported (n)	*63*	*63*	*9*	*54*	*3*	*34*	*26*
$CaCO_3$ flux	0.11‡	0.11‡	-	0.16‡	-	0.20*,‡	0.69*
Opal Only[b] *(n)*	*78*	*75*	*11*	*64*	*24*	*42*	*9*
Opal flux	0.44*	0.45*	-	0.54*	0.75*	0.47*	-
Ln (opal flux)	0.60*	0.62*	-	0.69*	0.64*	0.44*	-
Bulk flux	0.13	0.13	-	0.17	0.78*	0.26*	0.52
232Th flux	-	-	-	-	0.54*	-	0.64*
$\Delta^{14}C$[a]	-	-	-	-	0.22	0.22*	0.53
Depth	-	-	-	-	-	-	0.62
No Opal[c] *(n)*	*134*	*131*	*42*	*89*	*40*	*22*	*69*
Bulk flux	0.52*	0.56*	0.56*	0.50*	0.36*	0.39*	0.65*
^{232}Th flux	0.46*	0.52*	0.66*	0.31*	0.30*	0.41*	0.34*
$\Delta^{14}C$[a]	-	-	-	-	-	-	0.24*
Depth	-	-	-	-	-	-	-
Some Opal[d] *(n)*	*187*	*181*	*50*	*130*	*64*	*39*	*78*
Bulk Flux	0.48*	0.51*	0.51*	0.46*	0.57*	0.53*	0.65*
^{232}Th flux	0.45*	0.50*	0.64*	0.31*	0.34*	0.61*	0.35*
$\Delta^{14}C$[a]	-	-	-	-	0.13	0.15	0.26*
Depth	-	-	-	-	-	-	-

All reported R^2 are significant at the 95% confidence level.
*R^2 are $\geq$0.20 and significant at the 99% confidence level.
‡R is negative, inverse relationship suggested.
[a] $\Delta^{14}C$ refers to pre-industrial bottom water $\Delta^{14}C$ value interpolated from Holzer et al. (2021).
[b] *Opal Only* data set excludes samples without opal data.
[c] *No Opal* data set excludes all samples with opal data.
[d] *Some Opal* data set excludes samples with opal concentrations above 40 wt%.
[e] Ocean basins defined by preindustrial $\Delta^{14}C$ as follows: Atlantic > -125‰; Southern Ocean: -175 to -125‰; Pacific: < -175‰.

(Supplementary Table 1). In order to avoid overinterpretation of sparse data, we focus the remainder of our time series discussion on the compilation of data dating between 0 and 250 ka (Fig. 7). Synthesis of the global time series data set is complicated by the combination of climatically-driven changes in depositional environment (associated with variations in wet deposition of ^{10}Be to the sea surface, lithogenic input to the water column, and biogenic particle export, for example) as well as geomagnetically-driven variations in ^{10}Be production rates over time. We first examine the relationship between the measured ^{10}Be flux time series and magnetically-driven variations in the ^{10}Be production rate. Then, we apply a paleomagnetic correction for ^{10}Be production changes to each sample and evaluate the relationships between the corrected ^{10}Be flux time series and depositional environments observed in the core-top analysis.

3.3.1. *Impact of geomagnetic field intensity*

We do not observe any quantitative broad correlation between the global ^{10}Be flux time series data and ^{10}Be production rate variations estimated from paleomagnetic field intensity records over the last 250 kyr (Table 3; Fig. 7). Neither do we observe correlations between ^{10}Be flux data and paleomagnetic field intensity when data sets are grouped by basin, or when core top data points are excluded. This result is independent of the selection of the PISO-1500 (Channell et al., 2009) or the SINT-2000 (Valet et al., 2005) paleomagnetic intensity reconstruction.

Correlations between the PISO-1500-based relative ^{10}Be production rate and local ^{10}Be fluxes are slightly higher when evaluated on a site-by-site basis, rather than as a global data set (Supplementary Table 3). However, of the 33 timeseries in the global compilation with more than eight data points within the past 250 kyr, only three (MD04-2811 from the Portuguese Margin, NBP9802-5GC1 from the Pacific Southern Ocean, and AT26-19-09PC from the Northeast Pacific) exhibit correlations between ^{10}Be fluxes and relative ^{10}Be production rates with R^2 values in excess of 0.50 at the 95% confidence level ($R^2 = 0.62$, 0.50 and 0.56, respectively). The MD04-2811 ^{10}Be flux record may be especially sensitive to correlation with magnetically-induced variations in ^{10}Be flux because this record spans the period of time ~20-46 ka and was specifically generated to investigate the Laschamp excursion (Ménabréaz et al., 2011). In comparison, 29 of the 33 time series records examined do not exhibit any statistically significant or meaningful ($R^2 > 0.20$) correlation between ^{10}Be fluxes and relative ^{10}Be production rates (Supplementary Table 3). These weak correlations between PISO-1500-based relative ^{10}Be production rates and ^{10}Be fluxes are the lowest exhibited among the five parameters evaluated in the site-by-site correlation analysis (PISO-1500-based relative ^{10}Be production rate, bulk flux, ^{232}Th flux, opal flux, and $CaCO_3$ flux; Supplementary Table 3).

The apparent correlations calculated between the compiled ^{10}Be flux records and the PISO-1500 paleomagnetic intensity reconstruction may be reduced to some extent by offsets in the recorded timing of ^{10}Be flux changes in low sedimentation rate sediment cores, relative to the high-

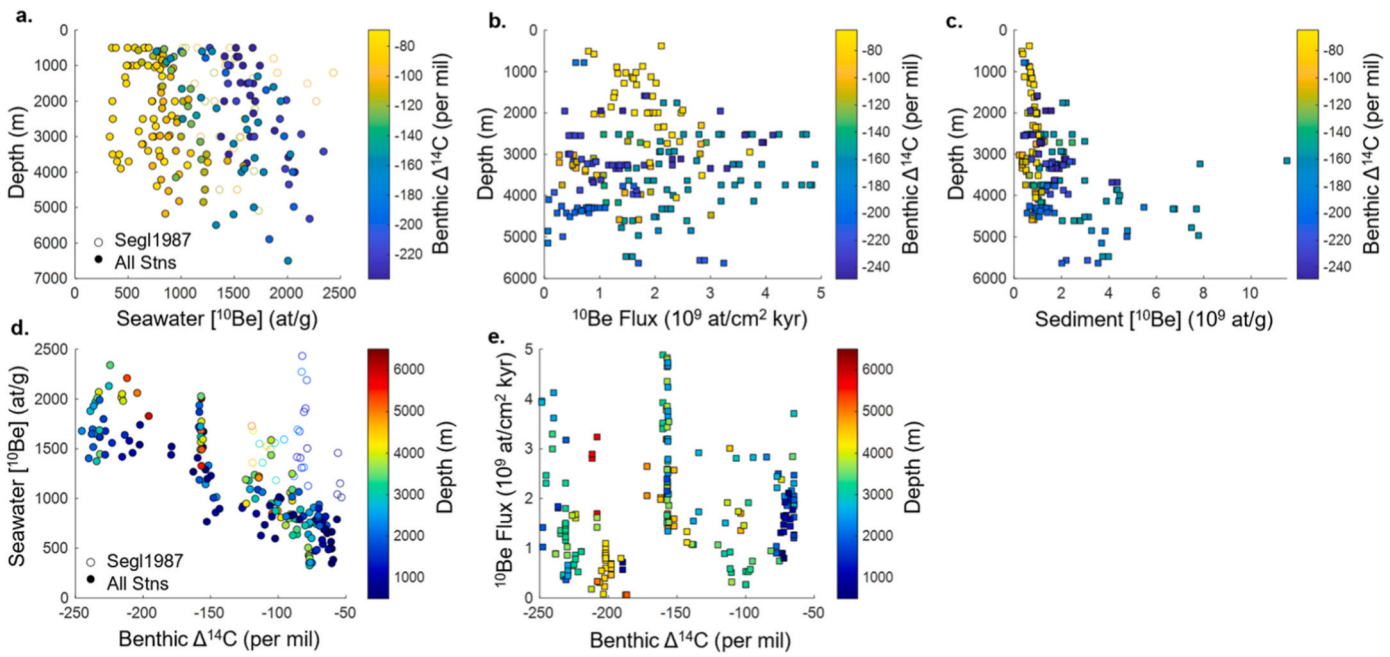

Fig. 5. Seawater and sediment ^{10}Be data versus depth and water mass age. (a-c) Depth versus (a) deep (>500 m) seawater dissolved ^{10}Be concentrations; (b) core-top/Holocene sedimentary ^{10}Be fluxes; (c) core-top/Holocene sedimentary ^{10}Be concentrations. Data are color coded based on the pre-industrial Δ^{14}C value of the underlying benthic water mass at each station and sediment core location for reference (Holzer et al., 2021). (d-e) Water mass age, approximated using pre-industrial water column and benthic water Δ^{14}C values interpolated from Holzer et al. (2021), versus (d) seawater dissolved ^{10}Be concentrations; (e) core-top/Holocene sedimentary ^{10}Be fluxes. Seawater and sediment data are color coded by water depth for reference. Seawater ^{10}Be data represent 35 station profiles as compiled by Deng et al. (2025) and references therein. Atlantic seawater ^{10}Be data from Segl et al., (1987) (open circles) do not appear consistent with the global trend indicated in (a) and (d). Deep water ^{10}Be concentrations increase linearly with water mass age ($R^2 = 0.48$ for full data set and $R^2 = 0.74$ when stations from Segl et al., 1987 are excluded).

resolution PISO-1500 stack, due to sediment core age model uncertainties and the compositional smoothing effect of bioturbation (e.g., Berger and Heath, 1968). Post depositional remanent magnetization of seafloor sediments can also cause a downward shift of the paleomagnetic intensity signal, relative to the ^{10}Be production rate change signal, as a function of a lock-in depth of ~10-15 cm that further complicates direct

Table 2
Pearson R^2 values for correlations between core-top/Holocene depth-normalized^{10}Be fluxes and assorted environmental parameters.

	Core Tops w/Flyers Removed[d]	Atlantic[e] Core Tops[d]	S. Ocean[e] Core Tops	Pacific[e] Core Tops
		Be flux/depth		
All Data (n)	*205*	*63*	*64*	*78*
Bulk flux	0.56*	0.36*	0.52*	0.83*
232Th flux	0.43*	0.47*	0.40*	0.62*
$\Delta^{14}C$[a]	0.12	0.44*	-	0.29*
$CaCO_3$ Reported (n)	*63*	*3*	*34*	*26*
$CaCO_3$ flux	0.12‡	-	0.20*,‡	0.58*
No Opal[b] *(n)*	*130*	*39*	*22*	*69*
Bulk flux	0.68*	0.34*	0.50*	0.83*
232Th flux	0.54*	0.40*	0.55*	0.61*
$\Delta^{14}C$[a]	0.22*	0.44*	0.30	0.26*
Some Opal[c] *(n)*	*180*	*63*	*39*	*78*
Bulk Flux	0.62*	0.36*	0.63*	0.83*
232Th flux	0.53*	0.46*	0.67*	0.62*
$\Delta^{14}C$[a]	0.13	0.44*	-	0.29*

All reported R^2 are significant at the 95% confidence level.
*R^2 are ≥0.20 and significant at the 99% confidence level.
‡R is negative, inverse relationship suggested.
[a] Δ^{14}C refers to pre-industrial bottom water Δ^{14}C value interpolated from Holzer et al. (2021).
[b] *No Opal* data set excludes all samples with opal data.
[c] *Some Opal* data set excludes samples with opal concentrations above 40 wt%.
[d] Data set excludes EN179 BC5 from 384 m water depth.
[e] Ocean basins defined by preindustrial Δ^{14}C as follows: Atlantic > −125‰; Southern Ocean: −175 to −125‰; Pacific: < −175‰.

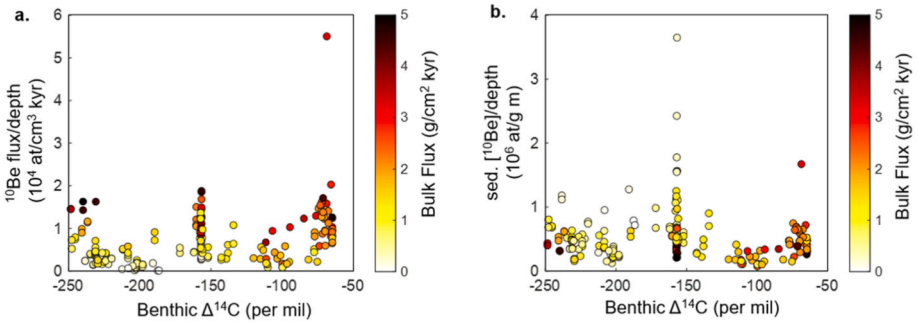

Fig. 6. Sediment ^{10}Be fluxes (a) and ^{10}Be concentrations (b) normalized by water depth as a function of water mass age, indicated by pre-industrial benthic water Δ^{14}C values interpolated from Holzer et al. (2021). Data are color coded by bulk sediment flux for reference. Color scale saturates at 5 g/cm^2 kyr to highlight variability on the low end of the spectrum.

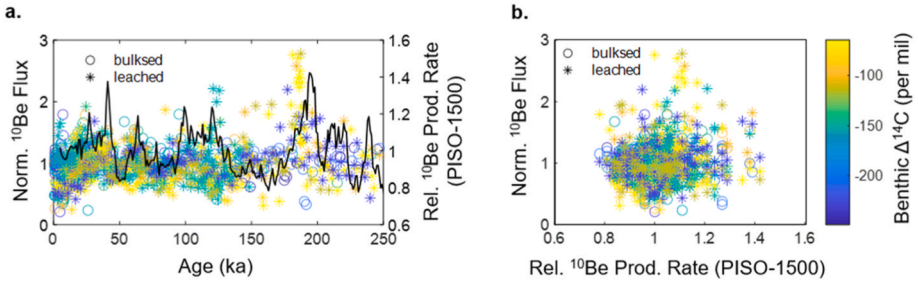

Fig. 7. Relationship between ^{10}Be flux data of the compiled time-series and the relative atmospheric ^{10}Be production rate. (a) Normalized time-series ^{10}Be flux data (markers), where the ^{10}Be flux values of each site are divided by the downcore average, and the relative ^{10}Be atmospheric production rate (black line; as in Fig. 2b). (b) Normalized time-series ^{10}Be flux data versus the relative ^{10}Be atmospheric production rate as in (a). The time-series ^{10}Be fluxes are normalized in this way for ease of comparison across varied depositional environments. The relative ^{10}Be production rate is calculated following the equations of Wagner et al. (2000) and the PISO-1500 magnetic paleo-intensity reconstruction (Channell et al., 2009). Open circles indicate ^{10}Be flux values derived from bulk sediment analysis, while stars indicate ^{10}Be flux values derived from leached sediment analysis. Data are color coded by pre-industrial bottom water Δ^{14}C values for each time-series core location for spatial reference (Holzer et al., 2021).

comparison of these two data sets (Channell and Guyodo, 2004; Suganuma et al., 2011). The extent of these effects is visually apparent in the normalized ^{10}Be flux time series records, determined by dividing the ^{10}Be flux values of each site by its downcore average (Fig. 7). The normalized ^{10}Be fluxes appear to exhibit variability between ~65 and 40 ka, across the Norwegian-Greenland Sea and Laschamp excursions, as well as the Iceland Basin excursion at ~190 ka, albeit offset by several thousand years from the PISO-1500-derived ^{10}Be production rate record (Fig. 7). Such sedimentological effects have less impact on comparisons of ^{10}Be flux data with other sediment component flux data in our analyses because all compositional measurements were generated on the same sediment core samples. Consequently, bioturbation and uncertainty in sediment sample ages would affect the sedimentary records of ^{10}Be flux and other sediment component fluxes to the same, or similar, degree at each site.

The lack of broad correlation between the compiled ^{10}Be flux data and paleomagnetic field intensity emphasizes the relatively minor role that production rate variations have played in governing global seafloor ^{10}Be fluxes over the last 250 kyr. This result does not imply that ^{10}Be production rates and ^{10}Be fluxes are not impacted by high frequency changes in geomagnetic field intensity over this interval, which has been well documented (e.g., Frank et al., 1997; Ménabréaz et al., 2011; Simon et al., 2016b; Simon et al., 2020). Rather, the absence of a broad correlation suggests that variations in local sediment fluxes and composition may complicate or overprint the production rate signal within sedimentary ^{10}Be flux records obtained from abyssal sediments.

Prior investigations have examined stacked ^{10}Be flux time series in order to identify the production rate signal from disparate sedimentary records (e.g., Frank et al., 1997). Our analysis suggests that such investigations of past changes in ^{10}Be production rate could be refined by correcting ^{10}Be flux data by site-specific changes in the depositional environment prior to stacking, as has recently been applied for reconstructions based on sedimentary ^{10}Be/^{9}Be ratios (Savranskaia et al., 2024). Notably, the relative importance of paleomagnetic field intensity on temporal variations in seafloor ^{10}Be fluxes may be higher in older records that span magnetic reversals, when relative field intensity changes were likely larger or sustained for longer periods of time (Valet et al., 2005, 2024; Channell et al., 2009).

3.3.2. *Impact of scavenging and other environmental factors*

The global sedimentary ^{10}Be flux time series data set exhibits much weaker correlations with bulk fluxes and lithogenic ^{232}Th fluxes (R^2 = 0.25 and the not meaningful 0.14, respectively) than observed in the core-top/Holocene data set alone, despite corrections for temporal variations in ^{10}Be production rates (Fig. 8, Table 3). When grouped by basin, correlations between ^{10}Be fluxes and bulk sediment fluxes in the Atlantic (n = 408), Southern Ocean (n = 390), and Pacific (n = 402) time series data remain weak, with R^2 values of 0.24, a not meaningful 0.10, and 0.25, respectively. The R^2 values of the correlations between ^{10}Be fluxes and ^{232}Th fluxes in the basin-specific Atlantic, Southern Ocean, and Pacific data sets are also negligible or very low (Table 3). In contrast, within individual sediment cores, the correlations between ^{10}Be fluxes and bulk and ^{232}Th fluxes can be much higher (Supplementary Table 3, Supplementary Fig. 3). Four cores (RC13-254, TT013-MC112, ODP Site 1208, and AT26-19-09PC) exhibit ^{10}Be-bulk flux correlation R^2 values greater than 0.60 at the 95% confidence level and five cores exhibit ^{10}Be-^{232}Th flux correlation R^2 values greater than 0.60 at the 95% confidence level (Supplementary Table 3).

Thus far, we have primarily examined the influence of lithogenic particles on ^{10}Be scavenging using ^{232}Th as a proxy for the lithogenic sediment fraction, as this proxy is well established (e.g., Kienast et al., 2016) and ^{232}Th data are available for all samples within the global

Table 3
Pearson R^2 values for correlations between sediment ^{10}Be fluxes and assorted environmental parameters within the 0-250 ka time series data.

	All Data 0-250 ka	Flyers Removed	Leached Samples	Bulk Samples	Atlantic[e] 0-250 ka	S. Ocean[e] 0-250 ka	Pacific[e] 0-250 ka
			^{10}Be Fluxes (no production rate correction)				
All Data (n)	*1243*	*1200*	*743*	*457*	*408*	*390*	*402*
Rel.^{10}Be Production Rate[a]	0.01	0.02	0.02	-	0.05	-	-
Rel. PM. Field Intensity[a]	0.01‡	0.01‡	0.03‡	-	0.03‡	-	-
			Site-normalized^{10}Be Fluxes (no production rate correction)				
Rel. PM. Field Intensity[a]	0.02‡	0.02‡	0.03‡	-	0.04‡	0.01‡	-
			^{10}Be Fluxes (production rate corrected)				
All Data (n)	*1243*	*1200*	*743*	*457*	*408*	*390*	*402*
Bulk flux	0.22*	0.25*	0.18	0.31*	0.24*	0.10	0.25*
^{232}Th flux	0.12	0.14	0.13	0.11	0.08	0.06	0.21*
$CaCO_3$ Reported (n)	*462*	*461*	*161*	*300*	*86*	*143*	*232*
$CaCO_3$ flux	0.08‡	0.09	-	0.22*,‡	-	0.05	0.07
Opal Only[b] (n)	*464*	*424*	*180*	*244*	*30*	*296*	*98*
Opal flux	0.12	0.14	-	0.60*	0.56*	0.03	0.39*
Ln (opal flux)	0.30*	0.40*	-	0.62*	0.52*	0.10	0.13
Bulk flux	0.12	0.12	-	0.38*	0.68*	0.05	0.19
^{232}Th flux	0.10	0.16	0.08	0.16	0.44*	0.28*	0.73*
No Opal[c] (n)	*779*	*766*	*563*	*213*	*378*	*94*	*304*
Bulk flux	0.39*	0.39*	0.30*	0.64*	0.23*	0.25*	0.25*
^{232}Th flux	0.29*	0.29*	0.21*	0.58*	0.07	0.22*	0.17
Some Opal[d] (n)	*1086*	*1035*	*666*	*379*	*408*	*235*	*402*
Bulk Flux	0.27*	0.29*	0.20*	0.34*	0.24*	0.16	0.25*
^{232}Th flux	0.23*	0.23*	0.16	0.34*	0.08	0.17	0.21*

All reported R^2 are significant at the 95% confidence level.
*R^2 are $\geq$0.20 and significant at the 99% confidence level.
‡R is negative, inverse relationship suggested.
[a] Relative^{10}Be production rate and relative paleomagnetic (PM) field intensity calculated from PISO-1500 (Channell et al., 2009) and Wagner et al. (2000).
[b] *Opal Only* data set excludes samples without opal data.
[c] *No Opal* data set excludes all samples with opal data.
[d] *Some Opal* data set excludes samples with opal concentrations above 40 wt%.
[e] Ocean basins defined by preindustrial Δ^{14}C as follows: Atlantic > −125‰; Southern Ocean: −175 to −125‰; Pacific: < −175‰.

compilation because they were generated in tandem with the measurements required for $^{230}Th_{XS}$-normalization. However, it is possible that small-scale spatial variability in the ^{232}Th concentration of lithogenic sediments (Kienast et al., 2016; McGee et al., 2016) may be partly responsible for the lower correlations between ^{10}Be fluxes and lithogenic ^{232}Th fluxes observed in the compiled time series data, relative to the strong correlations detected within individual records.

For samples with both $CaCO_3$ and opal data available, the lithogenic component can alternatively be estimated using a residual approach, in which the lithogenic concentration equals 100 wt% minus the $CaCO_3$ and opal concentrations, as percent of total. Within this limited subset of samples (n = 262; Supplementary Fig. 4), correlations between ^{10}Be fluxes and other sediment component fluxes are highest with the residual-based lithogenic flux (R^2 = 0.48), followed by opal flux (R^2 = 0.46), ^{232}Th flux (R^2 = 0.40), and bulk flux (R^2 = 0.39), and a weakly negative correlation is observed with $CaCO_3$ flux (R^2 = 0.28). This result supports the interpretation that ^{10}Be scavenging, and the resulting ^{10}Be flux, is more sensitive to the flux of specific mineralogic components (e.g., opal and lithogenic material) than it is to the bulk particle flux itself.

There are no meaningful correlations between ^{10}Be fluxes and $CaCO_3$ fluxes in the bulk time series data set or within the basin-specific data sets (Fig. 8, Table 3). This lack of correlation may result from the weaker ^{10}Be scavenging efficiency of $CaCO_3$, relative to opal or lithogenic particles. Alternatively, the lack of correlation between measured ^{10}Be fluxes and $CaCO_3$ fluxes may result from variable $CaCO_3$ preservation across regions and time, as the fate of scavenged ^{10}Be during dissolution events remains unknown. The absence of a clear relationship between ^{10}Be fluxes and $CaCO_3$ fluxes may be a primary driver of the lower correlations between ^{10}Be fluxes and bulk sediment fluxes observed in the time series data, especially among deep sites where $CaCO_3$ preservation is highly variable.

Evaluation of ^{10}Be flux correlations with opal fluxes is difficult in the time series data because opal data are only available for ~30% of the total samples, the majority of which are from Southern Ocean sediment cores (Fig. 8; Table 3). Of the individual time series with eight or more opal data points, four cores (V22-108, PS2082-1, RC13-254, and ODP Site 1208) exhibit ^{10}Be-opal flux correlation R^2 values greater than 0.60 at the 95% confidence level (Supplementary Table 3). All cores exhibiting strong correlations between ^{10}Be fluxes and opal fluxes in the time series analysis are located in the Atlantic sector of the Southern Ocean, with the exception of ODP Site 1208 from the northwest Pacific (Supplementary Fig. S3).

When samples with measured opal concentrations exceeding 40 wt% are eliminated from analysis, the global correlation between compiled ^{10}Be flux time series and bulk fluxes and ^{232}Th fluxes increases very slightly (R^2 = 0.29 and R^2 = 0.23, respectively). In the Southern Ocean time series data, the correlations between ^{10}Be fluxes and bulk and lithogenic ^{232}Th fluxes only become meaningful when all samples with

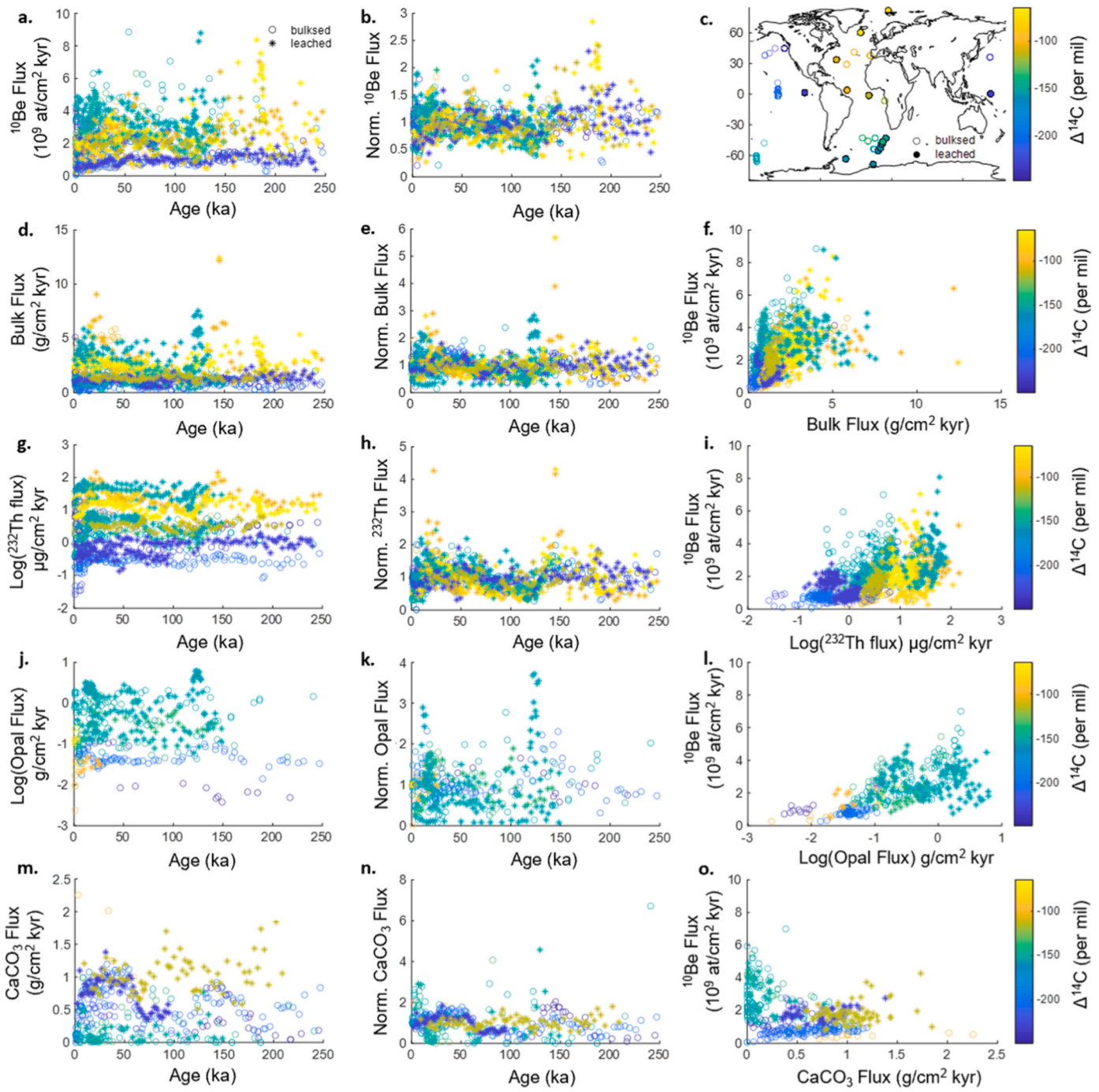

Fig. 8. Compilation time-series from 0 to 250 ka and correlation plots. (a) Time-series sediment ^{10}Be flux records; (b) Normalized ^{10}Be fluxes, where the ^{10}Be flux values of each site are divided by the downcore average; (c) pre-industrial bottom water Δ^{14}C values for each time-series core location for spatial reference (Holzer et al., 2021); (d) Bulk sediment fluxes; (e) normalized bulk sediment fluxes (as in b); (f) correlation of bulk sediment fluxes with ^{10}Be fluxes; (g) ^{232}Th fluxes; (h) normalized ^{232}Th fluxes; (i) correlation of ^{232}Th fluxes with ^{10}Be fluxes; (j) opal fluxes, where available; (k) normalized opal fluxes; (l) correlation of opal fluxes with ^{10}Be fluxes; (m) $CaCO_3$ fluxes, where available; (n) normalized $CaCO_3$ fluxes; (o) correlation of $CaCO_3$ fluxes with ^{10}Be fluxes. In all cases, ^{10}Be fluxes are corrected for magnetically-induced changes in the relative atmospheric ^{10}Be production rate over time (Section 2.3). Open circles indicate samples for which ^{10}Be data were derived from bulk sediment analysis, while stars indicate samples for which ^{10}Be data was derived from leached sediment analysis. Opal and ^{232}Th fluxes are plotted on a log scale, where indicated, for visual clarity. All fluxes are calculated using $^{230}Th_{XS}$-normalization. Data are color coded by pre-industrial bottom water Δ^{14}C values for each time-series core location for spatial reference.

opal data are eliminated (*No Opal* data subset, n = 94). This result suggests that temporal variations in the dominance of lithogenic vs. opal sediment inputs within individual records in the Southern Ocean strongly amplify the variability in observed ^{10}Be fluxes over time.

Unlike the global core-top data set, the correlations between ^{10}Be fluxes and particle fluxes (both bulk sediment flux and lithogenic ^{232}Th flux) within the time series data did not generally improve when ^{10}Be fluxes were normalized by sediment core water depth (Table 4). On a basin-specific basis, the Atlantic time series data sets exhibited weaker correlations between ^{10}Be fluxes and particle fluxes when sediment core water depth was accounted for, while the Southern Ocean and Pacific time series data showed an increase in these correlations (Table 4). The

R^2 values for correlations between depth-normalized ^{10}Be fluxes and bulk sediment fluxes, and ^{232}Th fluxes, were highest in the Pacific time series data (n = 402) and were 0.44 and 0.38, respectively.

We did not attempt investigation of potential relationships between ^{10}Be fluxes and water mass age in the time series data due to the low correlation observed in the core-top data set (see Section 3.2.4) and due to the increased uncertainties associated with reconstructing variable water mass ages in the paleorecord (e.g., Butzin et al., 2017; Rafter et al., 2022).

4. Discussion

A clear result of our analysis is that basin-scale differences in ^{10}Be deposition introduce variability within the sedimentary ^{10}Be records, such that a given bulk sediment flux may be associated with a range of different ^{10}Be fluxes, depending on where and when the samples are from. This basin-scale variability may reflect additional factors governing ^{10}Be fluxes, such as regional differences in settling particle composition (e.g., Chase et al., 2002; Frank et al., 2000), water mass geometry (Jeromson et al., 2024; Frank et al., 2009), and overlying seawater concentrations of dissolved ^{10}Be (e.g., White et al., 2019; Deng et al., 2025; Frank et al., 2002). Within the paleo record, global and local climate changes can cause these environmental factors to vary temporally, reducing the strength of the linear correlations observed between ^{10}Be flux and sediment particle fluxes observed in the core top data. Below we discuss the likely drivers of the basin-scale and temporal variability of the ^{10}Be flux data in more detail, as well as their implications for expanding applications of ^{10}Be as a paleoceanographic proxy.

4.1. Drivers of enhanced variability in paleo-^{10}Be flux records

On a global scale and within each ocean basin, the production rate-corrected timeseries of ^{10}Be fluxes exhibit more variability than is explainable by the water depth and particle flux relationships observed within the core-top/Holocene data alone (Tables 1 and 3).

Climate-driven changes in carbonate and opal accumulation and dissolution over the past 250 ka (Sayles et al., 2001; Bradtmiller et al., 2009; Howard and Prell, 1994; Anderson et al., 2008; Crowley, 1983) could introduce significant variability into the empirical relationships between ^{10}Be fluxes and other environmental parameters observed in the timeseries data, in contrast to the core-top/Holocene sediments. Due to the spread in K_d values associated with each major sediment component (Chase et al., 2002, 2003a; Frank et al., 2000; Lao et al., 1993; Kretschmer et al., 2011), any change in the relative input of lithogenic material, opal, or $CaCO_3$ to the sediments will impact the bulk ^{10}Be/particle ratio of that sample and thus alter the slope of the relationship between ^{10}Be fluxes and bulk fluxes through time. In addition, if sedimentary ^{10}Be is wholly or partially retained during carbonate or opal dissolution, then this would lead to the detection of elevated ^{10}Be/particle ratios relative to the original deposition signal and the magnitude of this effect would vary from region to region. Recent work has found a significant modern flux of dissolved ^{9}Be from continental margin sediments into the ocean (Deng et al., 2023), but the extent to which ^{10}Be may be lost from or retained in sediments during dissolution events requires further investigation. Comparative evaluation of K_d values estimated from seawater and in-situ particle pump samples with K_d values estimated from seafloor sediments, analogous to the work of Hayes et al. (2015) for ^{231}Pa and ^{230}Th, may provide a fruitful avenue for quantifying the impact of dissolution on sedimentary records of ^{10}Be.

In regions of high and variable opal production and preservation, like the Southern Ocean, one might expect the timeseries data to exhibit lower correlations between ^{10}Be fluxes and bulk sediment fluxes because opal deposition significantly increases the ^{10}Be/particle mass ratio of sediment relative to the lithogenic and carbonate fractions. Consequently, as climatic changes in upwelling conditions and deep-sea chemistry can cause big changes in opal concentrations within a sedimentary record, this effect would complicate the temporal relationship between ^{10}Be flux and bulk particle flux. However, the increased variability exhibited within the timeseries data is observed independently of whether one examines the entire suite of data, only samples with no measured opal contents, or only samples with opal contents less than or equal to 40 wt%. This result suggests that climatic changes in regional patterns of opal scavenging cannot explain all of the enhanced variability observed in the timeseries ^{10}Be flux data. Rather, we hypothesize that this additional variability is driven by temporal changes in regional seawater ^{10}Be inventories arising from changing climatic conditions.

Changes in the ^{10}Be residence time of seawater associated with a significant change in basin-scale particle fluxes could potentially drive climatic variations in seawater ^{10}Be concentrations. Climatic changes in atmospheric and ocean circulation, continental aridity, temperature, and nutrient supply, can cause widespread orbital and millennial-scale variations in both lithogenic and biogenic particle fluxes through the

Table 4
Pearson R^2 values for correlations between depth-normalized sediment ^{10}Be fluxes and assorted environmental parameters within the 0-250 ka time series data.

	All Data, No Flyers 0-250 ka[e]	Atlantic[f] 0-250 ka[e]	S. Ocean[f] 0-250 ka	Pacific[f] 0-250 ka
^{10}Be Flux/Depth (no production rate correction)				
All Data (n)	*1194*	*407*	*390*	*402*
Rel. ^{10}Be Production Rate[a]	0.02	0.03	0.01	-
Rel. PM. Field Intensity[a]	0.01‡	0.02‡	0.01‡	-
Site-normalized ^{10}Be Flux/Depth (no production rate correction)				
Rel. PM. Field Intensity[a]	0.01‡	0.01‡	0.01‡	-
^{10}Be Flux/Depth (production rate corrected)				
All Data (n)	*1194*	*407*	*390*	402
Bulk flux	0.23*	0.15	0.06	0.44*
^{232}Th flux	0.10	-	0.07	0.38*
$CaCO_3$ Reported (n)	*461*	*86*	*143*	*232*
$CaCO_3$ flux	0.16‡	-	0.16‡	0.03
Opal Only[b] (n)	*424*	*30*	*296*	*98*
Opal flux	0.10	0.66*	-	0.23*
Ln (opal flux)	0.39*	0.62*	0.11	0.02
Bulk flux	0.08	0.46*	0.01	0.14
^{232}Th flux	0.08	0.15	0.04	0.89*
No Opal[c] (n)	*765*	*377*	*94*	*304*
Bulk flux	0.32*	0.14	0.22*	0.48*
^{232}Th flux	0.15	-	0.20*	0.35*
Some Opal[d] (n)	*1034*	*407*	*235*	*402*
Bulk Flux	0.31*	0.15	0.27*	0.44*
^{232}Th flux	0.15	-	0.23*	0.38*

All reported R^2 are significant at the 95% confidence level.
*R^2 are ≥0.20 and significant at the 99% confidence level.
‡R is negative, inverse relationship suggested.
[a] Relative ^{10}Be production rate and relative paleomagnetic (PM) field intensity calculated from PISO-1500 (Channell et al., 2009) and Wagner et al. (2000).
[b] *Opal Only* data set excludes samples without opal data.
[c] *No Opal* data set excludes all samples with opal data.
[d] *Some Opal* data set excludes samples with opal concentrations above 40 wt%.
[e] Data set excludes EN179 BC5 from 384 m water depth.
[f] Ocean basins defined by preindustrial $\Delta^{14}C$ as follows: Atlantic > −125‰; Southern Ocean: −175 to −125‰; Pacific: < −175‰.

water column (e.g., Kienast et al., 2016; Albani et al., 2016; Anderson et al., 2009; Winckler et al., 2005). A recent time slice analysis of compiled $^{230}Th_{XS}$-normalized bulk sediment flux data suggested that the global sediment flux was ~1.5 times higher during the Last Glacial Maximum (LGM) than during the late Holocene, with a highest basin-scale increase of ~1.8-fold in the Atlantic (Costa et al., 2020). Such an increase in the global particle flux could increase the scavenging removal rate of ^{10}Be from seawater and thus decrease its residence time and the spatial patterns of deep water ^{10}Be concentrations. For example, higher Atlantic particle fluxes could lead to enhanced ^{10}Be scavenging removal from glacial Atlantic seawater, leading to less seawater ^{10}Be export via the deep ocean circulation into the Southern Ocean and Pacific basins and thus potentially lower ^{10}Be/particle ratios for glacial sediment in those downstream regions relative to core-top/Holocene values.

Ocean circulation and water mass geometry also impact the spatial pattern of seawater ^{10}Be concentrations and the net export of ^{10}Be from one basin to the next because of its nutrient-like distribution in the water column (e.g., Kusakabe et al., 1987; Deng et al., 2025). Consequently, temporal changes in overturning circulation, as suggested across glacial-interglacial cycles (Curry and Oppo, 2005; Basak et al., 2018) could introduce additional variability into sedimentary ^{10}Be/particle ratios, as well as the depth-dependence of ^{10}Be fluxes within each basin. For example, if a shoaling of low ^{10}Be North Atlantic Deep Water enabled a northward intrusion of high ^{10}Be waters into the North Atlantic during the LGM, then one would expect higher ^{10}Be/particle ratios in deep North Atlantic sediments, relative to the core-top/Holocene values, under comparable depositional settings. Atlantic sediments recovered above the shoaling line would not be expected to exhibit such a glacial increase in ^{10}Be/particle ratios.

4.2. Holocene-LGM time slice comparison

We investigate the impact of changing climatic conditions on ^{10}Be fluxes to the seafloor by comparing Holocene (0-10 ka) and Last Glacial Maximum (LGM; 18-24 ka) time slices using only samples from sediment cores with ^{10}Be flux data in each time slice (Fig. 9; Table 5). The time slice approach enables examination of global patterns of ^{10}Be fluxes within a distinct but narrow window of time, the LGM, and thus reduces confounding factors associated with temporally evolving oceanographic conditions. Even within the LGM time slice (n = 76), however, the global data do not exhibit a meaningful correlation between ^{10}Be fluxes and bulk sediment fluxes. In contrast, the Holocene time slice samples from the same cores exhibit a relatively strong correlation for the same relationship ($R^2 = 0.46$, n = 85). In general, the global LGM time slice ^{10}Be fluxes exhibit weaker correlations in all relationships, relative to the Holocene time slice data, including ^{232}Th fluxes and when samples with opal concentrations exceeding 40 wt% are eliminated (Table 5).

Climatic changes in relative $CaCO_3$ fluxes, or $CaCO_3$ concentrations, and/or carbonate dissolution across basins between the Holocene and LGM may also drive enhanced variability in the relationship between ^{10}Be fluxes and bulk sediment fluxes observed within the LGM time slice data by variably increasing (if $CaCO_3$ concentrations decrease) or decreasing (if $CaCO_3$ concentrations increase) bulk sediment ^{10}Be/particle ratios within the global snapshot (Fig. 5). However, the extent of this effect is difficult to assess at this time because $CaCO_3$ data is not available for the majority of the samples within the core-top or LGM time slices.

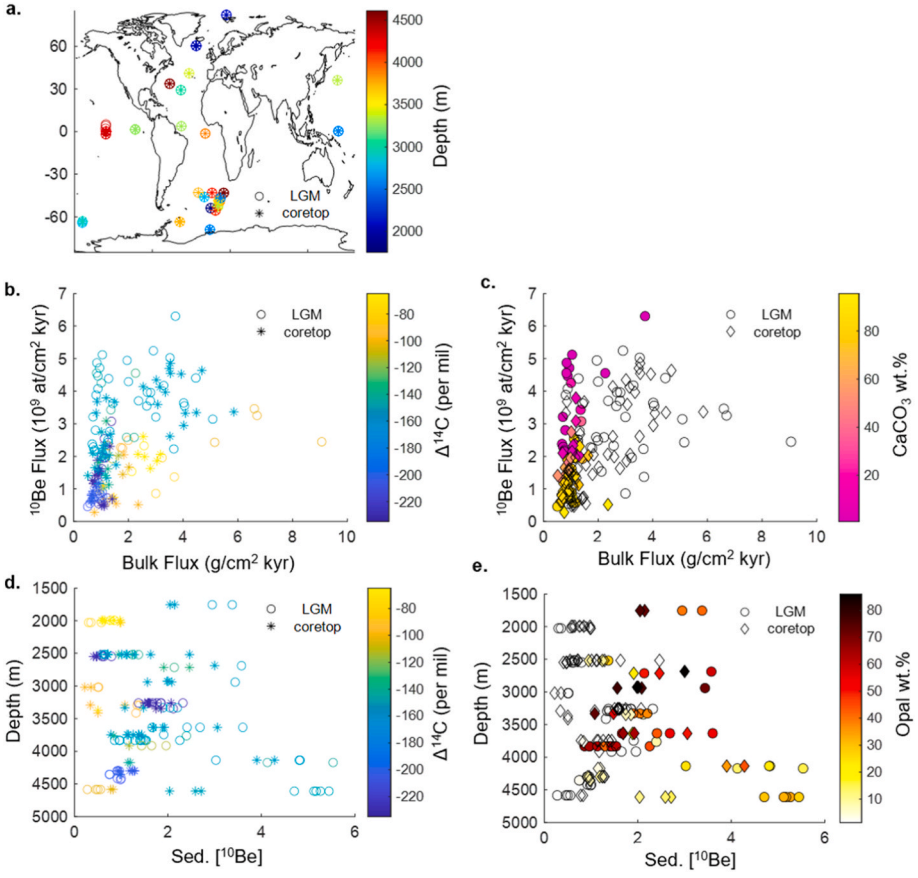

Fig. 9. Core-top/Holocene and Last Glacial Maximum (LGM) time slice data. (a) Location of sediment cores with ^{10}Be data in both the core-top/Holocene (0-10 ka; stars and diamonds) and LGM (18-24 ka; circles) time slice windows. Locations are color coded by depth for reference. (b) ^{10}Be fluxes as a function of bulk fluxes and water mass age, approximated by bottom water Δ^{14}C values interpolated from Holzer et al. (2021); (c) As in (b), but samples are color coded by $CaCO_3$ concentration; (d) time slice sedimentary ^{10}Be concentrations as a function of water depth and water mass age; (e) as in (d), but samples are color coded by opal concentration.

On the basin scale, the Atlantic and Southern Ocean time slice data exhibit the same pattern as the global time slices, including apparently weaker correlations with scavenging particle fluxes during the LGM than during the Holocene (Table 5). Interestingly, the Pacific time slice data exhibit the opposite pattern, with no significant correlations observed between ^{10}Be fluxes and bulk sediment fluxes during the Holocene (n = 25) and an improved relationship during the LGM ($R^2 = 0.44$, n = 19). This outcome may result from the sparse availability of Pacific samples suitable for the time slice comparison, as the broader Pacific core-top/Holocene data exhibit a much higher correlation between ^{10}Be fluxes and bulk sediment fluxes ($R^2 = 0.65$, n = 78, Table 1). The Pacific result may also be partially explained by the impact of bottom water chemistry on ^{10}Be fluxes to the sediments captured within the time slice samples, as the Pacific time slice data exhibit relatively strong correlations between depth-normalized ^{10}Be fluxes and pre-industrial benthic water radiocarbon values in both the Holocene ($R^2 = 0.47$, n = 25) and LGM (0.51, n = 19) time slices.

A basin-by-basin comparison of sediment ^{10}Be concentrations versus depth can help disentangle which regional processes drove the decreased correlation between ^{10}Be fluxes and bulk sediment fluxes within the LGM time slice (Fig. 9). The biggest difference in sediment ^{10}Be concentrations between Holocene and LGM time slice samples is observed in the Southern Ocean data, followed by the Atlantic, with the Pacific samples exhibiting the smallest changes in ^{10}Be concentrations between time slices. While changes in regional opal deposition, illustrated in Fig. 9 as changes in sediment opal concentration, may explain some of the variability observed in the Southern Ocean time slice data, we note that there are three cores from south of the polar front (RC13-259, NBP9802-5GC1, and PS1768-8) in which LGM samples exhibit higher ^{10}Be concentrations in sediments with either comparable or lower opal contents than Holocene samples from the same site. These cores also exhibit higher LGM ^{10}Be fluxes, relative to the Holocene, despite exhibiting lower or comparable LGM bulk flux values (Supplemental Table 2; Chase et al., 2003a; Frank et al., 2000; Kumar et al., 1995). Higher sediment ^{10}Be concentrations (or ^{10}Be/particle ratios) in lower opal content samples could reflect some retention of ^{10}Be following partial opal dissolution within the LGM sediment samples. Alternatively, this result may suggest that a higher seawater ^{10}Be inventory was available for scavenging during the LGM than during the Holocene. Such an increase in Southern Ocean seawater ^{10}Be concentrations could arise from enhanced ^{10}Be export from the Atlantic, reduced ^{10}Be export out of the Southern Ocean into the Pacific, or an increase in ^{10}Be delivery to the Southern Ocean via Antarctic meltwater inputs (Frank et al., 2000, 2002). Further investigation of the fluxes observed in the Southern Ocean sediment cores, including analysis of complementary circulation proxies such as neodymium and carbon isotopes, as well as independent characterization of the extent of opal dissolution in each sample via careful examination of diatom valves (e.

Table 5
Pearson R^2 values for correlations between sediment^{10}Be fluxes and assorted environmental parameters within the Core-top/Holocene (0-10ka) and Last Glacial Maximum (LGM; 18-24 ka) time slice samples.

	Core-top time slice	LGM time slice	Core-top time slice ATL[c]	LGM time slice ATL[c]	Core-top time slice SO[c]	LGM time slice SO[c]	Core-top time slice PAC[c]	LGM time slice PAC[c]
				^{10}Be flux (production rate corrected)[d]				
All data (n)	*85*	*76*	*17*	*17*	*43*	*40*	*25*	*19*
Bulk flux	0.46*	0.07	0.43*	0.30	0.47*	-	-	0.44*
^{232}Th flux	0.54*	-	-	0.19	0.52*	-	-	0.34*
$\Delta^{14}C$[a]	0.02	0.05	-	-	0.20*	-	0.23	0.34*
$CaCO_3$ Reported *(n)*	*36*	*33*	*3*	*5*	*18*	*14*	*15*	*14*
$CaCO_3$ flux	0.30*,‡	0.53*,‡	-	0.39‡	0.36*,‡	-	0.33	-
Some Opal[b] *(n)*	*73*	*56*	*17*	*17*	*31*	*20*	*25*	*19*
Bulk Flux	0.51*	-	0.43*	0.30	0.46*	-	-	0.44*
^{232}Th flux	0.63*	-	-	0.19	0.54*	-	-	0.34*
$\Delta^{14}C$[a]	0.02	0.06	-	-	0.41*	-	0.23	0.34*
				^{10}Be flux/depth (production rate corrected)[d]				
All data (n)	*85*	*76*	*17*	*17*	*43*	*40*	*25*	*19*
Bulk flux	0.51*	0.06	0.51*	-	0.47*	0.10	0.12	0.49*
^{232}Th flux	0.49*	-	-	-	0.51*	-	-	0.33
$\Delta^{14}C$[a]	0.06	0.09	0.58*	0.27	0.15	-	0.47*	0.51*
$CaCO_3$ Reported *(n)*	*36*	*33*	*3*	*5*	*18*	*14*	*15*	*14*
$CaCO_3$ flux	0.30*,‡	0.57*,‡	-	0.40‡	0.55*,‡	-	0.26	-
Some Opal[b] *(n)*	*73*	*56*	*17*	*17*	*31*	*20*	*25*	*19*
Bulk Flux	0.57*	-	0.51*	-	0.46*	0.15	0.12	0.49*
^{232}Th flux	0.56*	-	-	-	0.51*	0.18	-	0.33
$\Delta^{14}C$[a]	0.06	0.13	0.58*	0.27	0.36*	-	0.47[a]*	0.51*

All reported R^2 are significant at the 95% confidence level.
*R^2 are ≥0.20 and significant at the 99% confidence level.
‡R is negative, inverse relationship suggested.
[a] $\Delta^{14}C$ for both the core-top/Holocene and LGM time slice windows refers to pre-industrial bottom water $\Delta^{14}C$ value interpolated from Holzer et al. (2021).
[b] *Some Opal* data set excludes samples with opal concentrations above 40 wt%.
[c] Ocean basins defined by preindustrial $\Delta^{14}C$ as follows: Atlantic (ATL) > −125‰; Southern Ocean (SO): −175 to −125‰; Pacific (PAC): < −175‰.
[d] Relative^{10}Be production rate correction calculated from PISO-1500 (Channell et al., 2009) and Wagner et al. (2000).

g., Esper et al., 2010), would be greatly beneficial to understanding the patterns observed here.

In the Atlantic and Pacific time slices, there are fewer opal data available to assess the impact of changing scavenging particle type on sediment ^{10}Be concentrations. However, the Atlantic time slice data appear to exhibit a three-layer depth-dependence in the directionality of sediment ^{10}Be concentration changes between the Holocene and LGM (Fig. 9d). The shallowest (~2000 m) and deepest (~4500 m) time slice samples each exhibit lower ^{10}Be concentrations during the LGM, relative to the Holocene. In contrast, the mid-depth time slice samples (~3000 – 4000 m) tend to exhibit higher ^{10}Be concentrations during the LGM, relative to the Holocene. Such a varied depth-dependence in ^{10}Be changes would not be expected from a basin-wide change in scavenging removal associated with the LGM depositional environment. Rather, this interesting feature may result from a glacial difference in Atlantic water mass geometries or a glacial slow-down in the Atlantic Meridional Overturning Circulation (AMOC) as suggested by sedimentary records of benthic carbon isotopes (e.g., Duplessy et al., 1988; Oppo and Fairbanks, 1987; Curry and Oppo, 2005), authigenic neodymium (Rutberg et al., 2000; Howe et al., 2016), and ^{231}Pa/^{230}Th (e.g., McManus et al., 2004; Gherardi et al., 2009; Lippold et al., 2016), at intermediate water depths. We encourage more detailed exploration of the basin-specific glacial and interglacial differences in sedimentary ^{10}Be fluxes as a function of water mass, ocean chemistry, ocean circulation, and sediment dissolution using a multi-proxy approach, similar to the one presented by Pöppelmeier et al. (2023), in order to more thoroughly understand these observations, though such analyses are beyond the scope of this work.

4.3. Implications for Be as a paleo-proxy and paths forward

The global sedimentary ^{230}Th$_{XS}$-derived ^{10}Be flux compilation and analyses presented here demonstrate the extent to which sedimentary ^{10}Be records are influenced by oceanographic processes such as scavenging particle flux and composition, as well as ocean circulation and water mass geometry, and how these factors may have varied over time. Our results have significant implications for the current utilization of sedimentary ^{10}Be to infer past changes in the atmospheric ^{10}Be production rate as well as future applications of sedimentary ^{10}Be to better constrain past changes in oceanographic conditions. Below we discuss suggested best practices and paths forward for the refinement of ^{10}Be as paleoceanographic proxy.

When using sedimentary ^{10}Be fluxes to reconstruct past changes in atmospheric ^{10}Be production rates, either from changes in paleomagnetic field intensity (e.g., Frank et al., 1997) or from changes in the cosmic ray flux (e.g., Feige et al., 2013), one must account for the relatively large signal in ^{10}Be variability that may be caused by oceanographic processes relative to production rate changes themselves. In order to minimize the oceanographic and climatic impacts in such work, investigators are encouraged to develop ^{10}Be records in sediments from the deep Pacific gyres, or other regions where the combined temporal variations in particulate fluxes, sediment composition, and benthic water mass are expected to be relatively small. Further, investigators are encouraged to stack sedimentary ^{10}Be flux records from multiple locations, similar to the work of Frank et al. (1997), to avoid the possible over interpretation of local variability. However, we note that many climatic changes, such as glacial-interglacial cycles in particle flux and ocean circulation, may synchronously impact the seafloor ^{10}Be flux in the same direction across multiple regions. Due to the comparable chemical behavior of ^{10}Be and ^{9}Be, production rate reconstructions based on ^{10}Be/^{9}Be ratios are less sensitive to climatically-driven changes in Be scavenging than records based on ^{10}Be fluxes. Yet, sedimentary ^{10}Be/^{9}Be ratio records are not without their own complications, as temporal changes in the dissolved lithogenic ^{9}Be supply to the ocean and other environmental factors can provide distinct sources of natural variability into the production rate signal (Savranskaia et al., 2021, 2024; Simon et al., 2016b). Thus, as also concluded by recent ^{10}Be/^{9}Be studies (Savranskaia et al., 2021, 2024; Simon et al., 2016b), we encourage caution when interpreting major changes in ^{10}Be production rates from sedimentary ^{10}Be records that coincided with major changes in global climatic and environmental conditions.

Beyond production rate records, our global compilation encourages the continued development of sedimentary ^{10}Be as a paleoceanographic proxy with the potential to constrain past changes in ocean circulation and water mass geometry. The apparent sensitivity of sedimentary ^{10}Be fluxes to water mass, or water column, concentrations of dissolved ^{10}Be suggests that that such records could be used to reconstruct past changes in ocean circulation and water mass geometry (Fig. 10). While this method has been employed to distinguish marine and freshwater inputs along Antarctic margins and in the Arctic Ocean (Jeromson et al., 2024; White et al., 2019; Valletta et al., 2018; Sellén et al., 2009), this approach has not been widely applied to the vast abyssal ocean. During intervals when ^{10}Be production rate changes are independently constrained and the impact of sediment composition changes (which govern the bulk sediment K_d value) can be appropriately accounted for, sedimentary ^{10}Be flux records may prove to be fruitful for reconstructing water mass geometries through variable past climatic conditions. While all proxies carry their own unique sensitivities and complications, sedimentary ^{10}Be is analytically advantageous because it can be measured in carbonate-free sediments, where classical circulation proxies like stable carbon isotopes cannot be utilized. Further, the distinct affinities of ^{10}Be and ^{230}Th$_{XS}$ to particle scavenging suggest that ^{230}Th$_{XS}$-normalized ^{10}Be fluxes may be able to be exploited as a proxy for ocean circulation strength, analogous to previous uses of ^{231}Pa/^{230}Th (McManus et al., 2004; Waelbroeck et al., 2018; Jonkers et al., 2015). While recent work has highlighted the absence of a correlation between

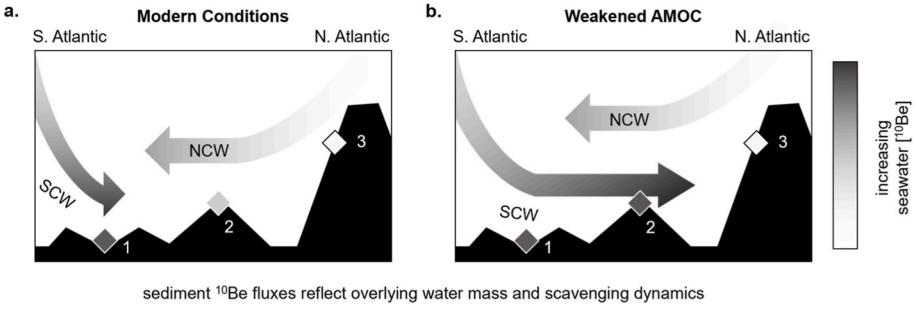

Fig. 10. Conceptual diagram of the impact of changing ocean circulation on sedimentary ^{10}Be fluxes. (a) Relative seawater ^{10}Be concentrations and underlying sediment ^{10}Be fluxes (diamonds numbered 1-3) along a latitudinal transect of the Atlantic under modern conditions; and (b) under a weakened Atlantic Meridional Overturning Circulation (AMOC) scenario. Sites 1-3 highlight locations in which sedimentary ^{10}Be fluxes are variably sensitive to recording past changes in AMOC strength. Northern Component Water (NCW) and Southern Component Water (SCW) labeled for clarity. Refinement of sedimentary ^{10}Be fluxes as a paleoceanographic circulation proxy will require additional constraints on temporal variations in scavenging dynamics, including particle composition and flux.

deep-sea dissolved $^{231}Pa/^{230}Th$ ratios and water mass age as a confounding issue with using $^{231}Pa/^{230}Th$ as a circulation proxy (Leal et al., 2025), deep-sea dissolved ^{10}Be concentrations do correlate with water mass age. Thus, sedimentary ^{10}Be fluxes may even have the potential to serve as a more straightforward paleoceanographic proxy than $^{231}Pa/^{230}Th$ and could be employed beyond the ~150 ka limit of short lived ^{231}Pa, with the caveat that the ^{10}Be production rate at each location and time is not as well constrained as that of $^{231}Pa/^{230}Th$. Ultimately, there is great possibility for sedimentary ^{10}Be fluxes, normalized by either $^{230}Th_{XS}$ or extraterrestrial helium-3 for deeper time applications, to help constrain ocean circulation changes throughout major climate reorganizations of the past ~10 million years.

Fundamentally important questions remain in our understanding of marine ^{10}Be systematics that will need to be addressed in order to improve applications of ^{10}Be as a paleoceanographic proxy. Is sedimentary ^{10}Be more sensitive to the full overlying water column inventory of dissolved ^{10}Be or only to the ^{10}Be concentration in the bottom water mass in which it accumulates? How sensitive are sediment ^{10}Be concentrations and $^{230}Th_{XS}$-normalized ^{10}Be fluxes to sediment dissolution? Do temporal variations in ^{10}Be fluxes primarily reflect changes in particulate scavenging or in ocean circulation and does the governing process vary between basins? These questions can be addressed by targeted studies that combine measurements of ^{10}Be and $^{230}Th_{XS}$ in core-top sediments and in the dissolved and particular phases of overlying seawater, as well as additional time series analyses to obtain ^{10}Be data in sediment cores that have already been well characterized in terms of particle composition, flux, dissolution and water mass history via other paleoceanographic proxies. Such work would also benefit from increased sampling coverage from the Indian Ocean and South Pacific basins, which would help to constrain the influence of water mass geometry and circulation history on seafloor ^{10}Be fluxes.

While new ^{10}Be analyses will provide fruitful constraints to test our hypotheses, an in-depth comparison of the current core-top/Holocene global sedimentary ^{10}Be flux data set in the frame of dynamic ocean models of Be systematics (e.g., Deng et al., 2025) would be an additional exciting avenue of future work in this field. Incorporation of sedimentary data into Be modeling would refine our understanding of the processes governing ^{10}Be deposition in the modern ocean, as well as provide a means to better constrain past ocean behavior using LGM or other paleo-time slice sedimentary ^{10}Be flux data (e.g., Pöppelmeier et al., 2023).

5. Conclusions

Globally, $^{230}Th_{XS}$-normalized ^{10}Be fluxes to seafloor sediments vary by nearly two orders of magnitude. If the dynamic processes responsible for this variability can be confidently identified and constrained, then sedimentary ^{10}Be fluxes could become a more widely beneficial palaeoceanographic proxy.

We have developed a global compilation of marine sedimentary $^{230}Th_{XS}$-normalized ^{10}Be flux data, including six new time series records generated in the frame of this study, in order to investigate the oceanographic and environmental factors governing ^{10}Be fluxes to the seafloor and to refine our ability to utilize sedimentary ^{10}Be as a paleoceanographic proxy. This approach was designed to assess ^{10}Be flux behavior under typical, open-ocean, abyssal conditions. The results of this study may not be representative of ^{10}Be deposition behavior in more complex scavenging environments, such as regions with bulk sediment fluxes in excess of 10 g/cm^2 kyr, regions with high levels of hydrothermal input or other unique mineralogic components, or regions where the $^{230}Th_{XS}$ constant flux proxy does not behave as expected.

Our analysis indicates that the primary factors driving the variability of ^{10}Be fluxes to the abyssal seafloor are (1) bulk sediment flux; (2) sediment composition, which alters the ^{10}Be/particle ratio (also known as ^{10}Be concentration) of the sediments; and (3) a combination of ocean basin and sediment core water depth. These factors combined can explain ~60% of the variability observed in global core-top ^{10}Be fluxes and up to 80% of the variability observed in the core-top data of each ocean basin. The influence of ocean basin and water depth on seafloor ^{10}Be fluxes likely reflects the sensitivity of sedimentary ^{10}Be to the water mass in which it accumulates and the overlying seawater ^{10}Be concentrations.

The empirical relationships observed in the core-top data between seafloor ^{10}Be fluxes and these three parameters (bulk sediment flux, sediment composition, and ocean basin/water depth) are weaker in the compiled time series data spanning the past 250 ka. These factors combined only explain ~30% of the variability of the global time series data set and ~15-45% of the variability within each ocean basin. We hypothesize that the enhanced variance observed in the time series ^{10}Be flux data is caused by climatically-driven changes in the available seawater ^{10}Be inventory within each water mass, associated with large scale changes in global particle flux and ocean circulation over time. However, the extent to which carbonate and opal dissolution impact sedimentary ^{10}Be records still merits further investigation.

The sensitivity of sedimentary ^{10}Be fluxes to overlying seawater ^{10}Be concentrations suggests that sedimentary ^{10}Be could be used to reconstruct past changes in basin-scale particle fluxes and ocean circulation, analogous to the shorter lived ^{231}Pa and ^{230}Th isotope systems, and encourages further investigation into the development of the refinement of ^{10}Be as a paleoceanographic proxy. Such investigations would benefit from enhanced spatial coverage of $^{230}Th_{XS}$-normalized sedimentary ^{10}Be time series, especially from the Indian Ocean basin, as well as additional paired water column-core top ^{10}Be analyses and the incorporation of sedimentary ^{10}Be data into dynamic ocean models of marine Be behavior in order to improve our understanding of how well sedimentary ^{10}Be records seawater ^{10}Be properties and how the processes governing this relationship vary with climatic and environmental changes.

CRediT authorship contribution statement

Jennifer Middleton: Conceptualization, Methodology, Formal analysis, Visualization, Writing – original draft. **Frank Pavia:** Investigation, Writing – review & editing. **Robert Anderson:** Investigation, Methodology, Writing – review & editing. **Roseanne Schwartz:** Investigation, Methodology, Writing – review & editing. **Martin Fleisher:** Investigation, Methodology. **Yong Lao:** Investigation, Methodology. **Yuxin Zhou:** Investigation, Methodology. **Christopher Kinsley:** Investigation, Methodology. **Joerg Schaefer:** Investigation, methodology. **Martin Frank:** Investigation, Methodology, Writing – review & editing. **Gisela Winckler:** Conceptualization, Investigation, Writing – review & editing.

Declaration of competing interest

The authors declare that they have no known competing financial interests or personal relationships that could have appeared to influence the work reported in this paper

Acknowledgements

All of the data in this paper are available in the references and supplementary tables. We are grateful to the authors of previous works who have made their isotope results and data tables readily available for future public use. We thank K. Costa and B. Reilly for fruitful discussion and two anonymous reviewers for their constructive suggestions. The new beryllium and thorium isotope data generated at LDEO, as well as the global compilation and analysis, were made possible via the financial support of US National Science Foundation grants OCE-1933837 and AGS-1338832.

Appendix A. Supplementary data

Supplementary data to this article can be found online at https://doi.org/10.1016/j.quascirev.2026.109922.

Data availability

All data and/or code is contained within the submission.

References

Albani, S., Mahowald, N.M., Murphy, L.N., Raiswell, R., Moore, J.K., Anderson, R.F., McGee, D., Bradtmiller, L.I., Delmonte, B., Hesse, P.P., Mayewski, P.A., 2016. Paleodust variability since the last glacial maximum and implications for iron inputs to the ocean. Geophys. Res. Lett. 43, 3944–3954. https://doi.org/10.1002/2016GL067911.

Anderson, R., Broecker, W., Trumbore, S., Hofmann, H., Wolfli, W., 1990. Boundary scavenging in the Pacific Ocean: a comparison of 10Be and 231Pa. Earth Planet Sci. Lett. 96, 287–304.

Anderson, R.F., Ali, S., Bradtmiller, L.I., Nielsen, S.H.H., Fleisher, M.Q., Anderson, B.E., Burckle, L.H., 2009. Wind-driven upwelling in the Southern Ocean and the deglacial rise in atmospheric CO2. Science 323, 1442–1448 (1979).

Anderson, R.F., Fleisher, M.Q., Biscaye, P.E., Kumar, N., Dittrich, B., Kubik, P., Suter, M., 1994. Anomalous boundary scavenging in the middle Atlantic bight: evidence from 230Th, 231Pa, 10Be and 210Pb. Deep-Sea Research II 41, 537–561.

Anderson, R.F., Fleisher, M.Q., Lao, Y., 2006. Glacial-interglacial variability in the delivery of dust to the central equatorial Pacific Ocean. Earth Planet Sci. Lett. 242, 406–414. https://doi.org/10.1016/j.epsl.2005.11.061.

Anderson, R.F., Fleisher, M.Q., Lao, Y., Winckler, G., 2008. Modern CaCO3 preservation in equatorial Pacific sediments in the context of late-pleistocene glacial cycles. Mar. Chem. 111, 30–46. https://doi.org/10.1016/j.marchem.2007.11.011.

Balco, G., Shuster, D.L., 2009. Production rate of cosmogenic 21Ne in quartz estimated from 10Be, 26Al, and 21Ne concentrations in slowly eroding Antarctic bedrock surfaces. Earth Planet Sci. Lett. 281, 48–58. https://doi.org/10.1016/j.epsl.2009.02.006.

Balter-Kennedy, A., Schaefer, J.M., Schwartz, R., Lamp, J.L., Penrose, L., Middleton, J., Hanley, J., Tibari, B., Blard, P.H., Winckler, G., Hidy, A.J., Balco, G., 2023. Cosmogenic 10Be in pyroxene: laboratory progress, production rate systematics, and application of the 10Be-3He nuclide pair in the Antarctic dry valleys. Geochronology 5, 301–321. https://doi.org/10.5194/gchron-5-301-2023.

Basak, C., Fröllje, H., Lamy, F., Gersonde, R., Benz, V., Anderson, R.F., Molina-Kescher, M., Pahnke, K., 2018. Breakup of last glacial deep stratification in the South Pacific. Science 359, 900–904, 1979.

Berelson, W.M., Anderson, R.F., Dymond, J., Demaster, D., Hammond, D.E., Collier, R., Honjo, S., Leinen, M., Mcmanus, J., Pope, R., Smith, C., Stephens, M., 1997. Biogenic budgets of particle rain, benthic remineralization and sediment accumulation in the equatorial Pacific. Deep-Sea Research II 44, 2251–2282.

Berger, W.H., Heath, G.R., 1968. Vertical mixing in pelagic sediments. J. Mar. Res. 26, 134–143.

Bernsdorff, F., 2008. Rekonstruktion Der Erdmagnetfeldstärke Der Vergangenen 300.000 Jahre Über Den Kosmogenen Tracer 10 Be Aus Atlantischen Tiefseesedimenten (ODP-Sites 983 Und 1063). Ruprecht-Karls-Universitat, Heidelberg.

Bourles, D., Raisbeck, G.M., Yiou, F., 1989. 10Be and 9Be in marine sediments and their potential for dating. Geochim. Cosmochim. Acta 53, 443–452.

Bradtmiller, L.I., Anderson, R.F., Fleisher, M.Q., Burckle, L.H., 2009. Comparing glacial and Holocene opal fluxes in the Pacific sector of the Southern Ocean. Paleoceanography 24. https://doi.org/10.1029/2008PA001693. PA2214.

Bralower, T.J., Premoli Silva, I., Malone, M.J., 2002. Volume 198 scientific results. Proc. Ocean Drill. Progr. Sci. Results 198.

Channell, J.E.T., Kanamatsu, T., Sato, T., Stein, R., Alvarez Zarikian, C.A., Malone, M.J., 2006. Site U1313. In: Proceedings of the Integrated Ocean Drilling Program, 303/306.

Channell, J.E.T., Xuan, C., Hodell, D.A., 2009. Stacking paleointensity and oxygen isotope data for the last 1.5 Myr (PISO-1500). Earth Planet Sci. Lett. 283, 14–23. https://doi.org/10.1029/2001pa000733.

Butzin, M., Koehler, P., Lohmann, G., 2017. Marine radiocarbon reservoir age simulations for the past 50,000 years. Geophys. Res. Lett. 44, 8473–8480. https://doi.org/10.1002/2017GL074688.

Channell, J.E.T., Guyodo, Y., 2004. The Matuyama Chronozone at ODP site 982 (Rockall bank): evidence for decimeter-scale magnetization lock-in depths. In: Timescales of the Paleomagnetic Field, pp. 205–219.

Chase, Z., Anderson, R.F., Fleisher, M.Q., Kubik, P.W., 2003a. Accumulation of biogenic and lithogenic material in the Pacific sector of the Southern Ocean during the past 40,000 years. Deep-Sea Res. Part II 50, 799–832. https://doi.org/10.1016/S0967-0645(02)00595-7.

Chase, Z., Anderson, R.F., Fleisher, M.Q., Kubik, P.W., 2003b. Scavenging of 230Th, 231Pa and 10Be in the Southern Ocean (SW Pacific sector): the importance of particle flux, particle composition and advection. Deep-Sea Res. Part II 50, 739–768. https://doi.org/10.1016/S0967-0645(02)00593-3.

Chase, Z., Anderson, R.F., Fleisher, M.Q., Kubik, P.W., 2002. The influence of particle composition and particle flux on scavenging of Th, Pa and be in the ocean. Earth Planet Sci. Lett. 204, 215–229.

Chmeleff, J., von Blanckenburg, F., Kossert, K., Jakob, D., 2010. Determination of the 10Be half-life by multicollector ICP-MS and liquid scintillation counting. Nucl. Instrum. Methods Phys. Res. B 268, 192–199. https://doi.org/10.1016/j.nimb.2009.09.012.

Christl, M., Lippold, J., Steinhilber, F., Bernsdorff, F., Mangini, A., 2010. Reconstruction of global 10Be production over the past 250ka from highly accumulating Atlantic drift sediments. Quat. Sci. Rev. 29, 2663–2672. https://doi.org/10.1016/j.quascirev.2010.06.017.

Christl, M., Mangini, A., Kubik, P.W., 2007. Highly resolved Beryllium-10 record from ODP site 1089-A global signal? Earth Planet Sci. Lett. 257, 245–258. https://doi.org/10.1016/j.epsl.2007.02.035.

Christl, M., Strobl, C., Mangini, A., 2003. Beryllium-10 in deep-sea sediments: a tracer for the Earth's magnetic field intensity during the last 200,000 years. Quat. Sci. Rev. 22, 725–739. https://doi.org/10.1016/S0277-3791(02)00195-6.

Costa, K., McManus, J., 2017. Efficacy of 230Th normalization in sediments from the Juan de Fuca Ridge, northeast Pacific Ocean. Geochim Cosmochim Acta 197, 215–225. https://doi.org/10.1016/j.gca.2016.10.034.

Costa, K.M., 2018. Geochemical Fingerprints of Paleoceanographic Variability in the Subarctic Pacific over the Last 500,000 Years. Columbia University.

Costa, K.M., Hayes, C.T., Anderson, R.F., Pavia, F.J., Bausch, A., Deng, F., Dutay, J.C., Geibert, W., Heinze, C., Henderson, G., Hillaire-Marcel, C., Hoffmann, S., Jaccard, S. L., Jacobel, A.W., Kienast, S.S., Kipp, L., Lerner, P., Lippold, J., Lund, D., Marcantonio, F., McGee, D., McManus, J.F., Mekik, F., Middleton, J.L., Missiaen, L., Not, C., Pichat, S., Robinson, L.F., Rowland, G.H., Roy-Barman, M., Tagliabue, A., Torfstein, A., Winckler, G., Zhou, Y., 2020. 230Th normalization: new insights on an essential tool for quantifying sedimentary fluxes in the modern and Quaternary ocean. Paleoceanogr. Paleoclimatol. 35. https://doi.org/10.1029/2019PA003820 e2019PA003820.

Costa, K.M., McManus, J.F., Anderson, R.F., 2018. Paleoproductivity and stratification across the subarctic Pacific over glacial-interglacial cycles. Paleoceanogr. Paleoclimatol. 33, 914–933. https://doi.org/10.1029/2018PA003363.

Costa, K.M., McManus, J.F., Boulahanis, B., Carbotte, S.M., Winckler, G., Huybers, P.J., Langmuir, C.H., 2016. Sedimentation, stratigraphy and physical properties of sediment on the Juan de Fuca Ridge. Mar. Geol. 380, 163–173. https://doi.org/10.1016/j.margeo.2016.08.003.

Costa, K.M., Pavia, F.J., Piecuch, C.G., McManus, J.F., Weinstein, G.A., 2024. Pelagic sedimentation rates in the North Pacific using Thorium-230 depth profiling. Geochim Cosmochim Acta 369, 126–140. https://doi.org/10.1016/j.gca.2023.11.020.

Crowley, T.J., 1983. Calcium-carbonate preservation patterns in the central north Atlantic during the last 150,000 years. Mar. Geol. 51, 1–14.

Curry, W.B., Oppo, D.W., 2005. Glacial water mass geometry and the distribution of δ 13C of ΣCO2 in the Western Atlantic Ocean. Paleoceanography 20, 1–12. https://doi.org/10.1029/2004PA001021.

Deng, K., de Souza, G.F., Du, J., 2025. Modern oceanic cycle of beryllium isotopes assessed using a data-constrained biogeochemical model. Geochim Cosmochim Acta 389, 186–199. https://doi.org/10.1016/j.gca.2024.10.025.

Deng, K., Rickli, J., Suhrhoff, T.J., Du, J., Scholz, F., Severmann, S., Yang, S., Mcmanus, J., Vance, D., 2023. Dominance of benthic fluxes in the oceanic beryllium budget and implications for paleo-denudation records. Sci. Adv. 9 eadg3702.

Deng, K., Wittmann, H., von Blanckenburg, F., 2020. The depositional flux of meteoric cosmogenic 10Be from modeling and observation. Earth Planet Sci. Lett. 550, 116530. https://doi.org/10.1016/j.epsl.2020.116530.

Duplessy, J.C., Shackleton, N.J., Fairbanks, R.G., Labeyrie, L., Oppo, D., Kallel, N., 1988. Deepwater source variations during the last climatic cycle and their impact on the global deepwater circulation. Paleoceanography 3, 343–360. https://doi.org/10.1029/PA003i003p00343.

Eisenhauer, A., Spielhagen, R.F., Frank, M., Hentzschel, G., Mangini, A., Kubik, P.W., Dittrich-Hannen, B., Billen, T., 1994. 10Be records of sediment cores from high northern latitudes: implications for environmental and climatic changes. Earth Planet Sci. Lett. 124, 171–184.

Esper, O., Gersonde, R., Kadagies, N., 2010. Diatom distribution in southeastern Pacific surface sediments and their relationship to modern environmental variables. Palaeogeogr. Palaeoclimatol. Palaeoecol. 287, 1–27. https://doi.org/10.1016/j.palaeo.2009.12.006.

Feige, J., Wallner, A., Fifield, L.K., Korschinek, G., Merchel, S., Rugel, G., Steier, P., Winkler, S.R., Golser, R., 2013. AMS measurements of cosmogenic and supernova-ejected radionuclides in deep-sea sediment cores. In: Heavy Ion Accelerator Symposium. EPJ Web of Conferences, 03003. https://doi.org/10.1051/C.

Fleisher, M.Q., Anderson, R.F., 2003. Assessing the collection efficiency of Ross sea sediment traps using 230Th and 231Pa. Deep Sea Res 2 Top Stud Oceanogr 50, 693–712. https://doi.org/10.1016/S0967-0645(02)00591-X.

Frank, M., Backman, J., Jakobsson, M., Moran, K., O'Regan, M., King, J., Haley, B.A., Kubik, P.W., Garbe-Schönberg, D., 2008. Beryllium isotopes in central Arctic Ocean sediments over the past 12.3 million years: stratigraphic and paleoclimatic implications. Paleoceanography 23. https://doi.org/10.1029/2007PA001478. PA1S02.

Frank, M., Eckhardt, J.-D., Eisenhauer, A., Kubik, P.W., Dittrich-Hannen, B., Segl, M., Mangini, A., 1994. Beryllium 10, thorium 230, and protactinium 231 in Galapagos microplate sediments: implications of hydrothermal activity and paleoproductivity changes during the last 100,000 years. Paleoceanography 9, 559–578. https://doi.org/10.1029/94PA01132.

Frank, M., Eisenhauer, A., Bonn, W.J., Walter, P., Grober, H., Kubik, P.W., Dittrich-Hannen, B., Mangini, A., 1995. Sediment redistribution versus paleoproductivity change: Weddell Sea margin sediment stratigraphy and biogenic particle flux of the

last 250,000 years deduced from 230Thex, 10Be and biogenic barium profiles. Earth Planet Sci Lett 136, 559–573.
Frank, M., Gersonde, R., Rutger Van Der Loeff, M., Bohrmann, G., Nürnberg, C.C., Kubik, P.W., Suter, M., Mangini, A., 2000. Similar glacial and interglacial export bioproductivity in the Atlantic sector of the Southern Ocean: multiproxy evidence and implications for glacial atmospheric CO2. Paleoceanography 15, 642–658. https://doi.org/10.1029/2000PA000497.
Frank, M., Mangini, A., Gersonde, R., Rutgers Van Der Loeff, M., Kuhn, G., Rundsch, G., 1996. Late Quaternary Sediment Dating and Quantification of Lateral Sediment Redistribution Applying 230 Th Ex : a Study from the Eastern Atlantic Sector of the Southern Ocean. Springer-Verlag.
Frank, M., Porcelli, D., Andersson, P., Baskaran, M., Björk, G., Kubik, P.W., Hattendorf, B., Guenther, D., 2009. The dissolved Beryllium isotope composition of the Arctic Ocean. Geochim Cosmochim Acta 73, 6114–6133. https://doi.org/10.1016/j.gca.2009.07.010.
Frank, M., Rutgers Van Der Loeff, M.M., Kubik, P.W., Mangini, A., 2002. Quasi-conservative behaviour of 10 be in deep waters of the Weddell Sea and the Atlantic sector of the Antarctic circumpolar current. Earth Planet Sci. Lett. 201, 171–186.
Frank, M., Schwarz, B., Baumann, S., Kubik, P.W., Suter, M., Mangini, A., 1997. A 200 kyr record of cosmogenic radionuclide production rate and geomagnetic field intensity from loBe in globally stacked deep-sea sediments. Earth Planet Sci. Lett. 149, 12–29.
Geibert, W., Matthiessen, J., Stimac, I., Wollenburg, J., Stein, R., 2021. Glacial episodes of a freshwater Arctic Ocean covered by a thick ice shelf. Nature 590, 97–102. https://doi.org/10.1038/s41586-021-03186-y.
Gherardi, J.M., Labeyrie, L., Nave, S., Francois, R., McManus, J.F., Cortijo, E., 2009. Glacial-interglacial circulation changes inferred from231Pa/230Th sedimentary record in the North Atlantic region. Paleoceanography 24, PA2204. https://doi.org/10.1029/2008PA001696.
Graham, I., Ditchburn, R., Barry, B., 2003. Atmospheric deposition of 7Be and 10Be in New Zealand rain (1996-98). Geochim Cosmochim Acta 67, 361–373.
Gu, Z.Y., Lal, D., Liu, T.S., Southon, J., Caffee, M.W., Guo, Z.T., Chen, M.Y., 1996. Five million year 10Be record in Chinese loess and red-clay: climate and weathering relationships. Earth Planet Sci. Lett. 144, 273–287.
Hayes, C.T., Anderson, R.F., Fleisher, M.Q., Vivancos, S.M., Lam, P.J., Ohnemus, D.C., Huang, K.F., Robinson, L.F., Lu, Y., Cheng, H., Edwards, R.L., Moran, S.B., 2015. Intensity of Th and Pa scavenging partitioned by particle chemistry in the North Atlantic Ocean. Mar. Chem. 170, 49–60. https://doi.org/10.1016/j.marchem.2015.01.006.
Heikkilä, U., von Blanckenburg, F., 2015. The global distribution of Holocene meteoric 10 be fluxes from atmospheric models. Distribution maps for terrestrial Earth surface applications. https://doi.org/10.5880/GFZ.3.4.2015.001.
Henderson, G.M., Anderson, R.F., 2003. The U-series toolbox for paleoceanography. In: Reviews in Mineralogy and Geochemistry, pp. 493–531.
Henken-Mellies, W.U., Beer, J., Heller, F., Hsü, K.J., Shen, C., Bonani, G., Hofmann, H.J., Suter, M., Wölfli, W., 1990. 10Be and 9Be in South Atlantic DSDP site 519: relation to geomagnetic reversals and to sediment composition. Earth Planet Sci. Lett. 98, 267–276.
Holzer, M., DeVries, T., de Lavergne, C., 2021. Diffusion controls the ventilation of a Pacific Shadow zone above abyssal overturning. Nat. Commun. 12, 4348. https://doi.org/10.1038/s41467-021-24648-x.
Howard, W.R., Prell, W.L., 1994. Late Quaternary CaCO3 production and preservation in the Southern Ocean: implications for oceanic and atmospheric carbon cycling. Paleoceanography 9, 453–482. https://doi.org/10.1029/93PA03524.
Howe, J.N.W., Piotrowski, A.M., Noble, T.L., Mulitza, S., Chiessi, C.M., Bayon, G., 2016. North Atlantic deep water production during the last glacial maximum. Nat. Commun. 7, 11765. https://doi.org/10.1038/ncomms11765.
Jeromson, M.R., Fujioka, T., Fink, D., Simon, K., Smith, J., Hillenbrand, C.D., Kuhn, G., Post, A.L., Sánchez-Palacios, J.T., Blaxell, M., Enge, T.G., White, D.A., 2024. Circumpolar deep water upwelling is a primary source of 10Be in Antarctic continental shelf sediments. Glob Planet Change 236, 104424. https://doi.org/10.1016/j.gloplacha.2024.104424.
Jonkers, L., Barker, S., Hall, I.R., Prins, M.A., 2015. Correcting for the influence of ice-rafted detritus on grain size-based paleocurrent speed estimates. Paleoceanography 30, 1347–1357. https://doi.org/10.1002/2015PA002830.
Kaste, J.M., Baskaran, M., 2012. Meteoric 7Be and 10Be as process tracers in the environment. In: Handbook of Environmental Isotope Geochemisry. Springer-Verlag Berlin Heidelberg, pp. 61–85.
Kienast, S.S., Winckler, G., Lippold, J., Albani, S., Mahowald, N.M., 2016. Tracing dust input to the global ocean using thorium isotopes in marine sediments: thoromap. Glob. Biogeochem. Cycles 30, 1526–1541. https://doi.org/10.1002/2016GB005408.
Kinsley, C.W., Bradtmiller, L.I., Zhang, Y., Perala-Dewey, J., McGee, D., 2022. Ocean-atmosphere changes in the midlatitude North Pacific over the last 330 ka: dust, biogenic sediment and authigenic uranium accumulation at Shatsky rise. (version 1). Zenodo [WWW Document]. https://doi.org/10.5281/zenodo.6791725.
Koll, D., Lachner, J., Beutner, S., Fichter, S., Merchel, S., Rugel, G., Slavkovská, Z., Vivo-Vilches, C., Winkler, S., Wallner, A., 2025. A cosmogenic 10Be anomaly during the late Miocene as independent time marker for marine archives. Nat. Commun. 16, 866. https://doi.org/10.1038/s41467-024-55662-4.
Korschinek, G., Bergmaier, A., Faestermann, T., Gerstmann, U.C., Knie, K., Rugel, G., Wallner, A., Dillmann, I., Dollinger, G., von Gostomski, C.L., Kossert, K., Maiti, M., Poutivtsev, M., Remmert, A., 2010. A new value for the half-life of 10Be by heavy-ion elastic recoil detection and liquid scintillation counting. Nucl. Instrum. Methods Phys. Res. B 268, 187–191. https://doi.org/10.1016/j.nimb.2009.09.020.
Kretschmer, S., Geibert, W., Rutgers van der Loeff, M.M., Schnabel, C., Xu, S., Mollenhauer, G., 2011. Fractionation of 230Th, 231Pa, and 10Be induced by particle size and composition within an opal-rich sediment of the Atlantic Southern Ocean. Geochim Cosmochim Acta 75, 6971–6987. https://doi.org/10.1016/j.gca.2011.09.012.
Kroenke, L.W., Berger, W.H., Janecek, T.R., 1991. Site 806. Proceedings of the Ocean Drilling Program, Initial Reports 130, 291–367.
Ku, T.L., Kusakabe, M., Measures, C.I., Southon, J.R., Cusimano, G., Vogela, J.S., Nelson, D.E., Nakaya, S., 1990. Beryllium isotope distribution in the Western North Atlantic: a comparison to the Pacific. Deep-Sea Res. 37, 795–808.
Kumar, N., Anderson, R.F., Mortlock, R.A., Froelich, P.N., Kubik, P., Dittrich-Hannen, B., Suter, M., 1995. Increased biological productivity and export production in the glacial Southern Ocean. Nature 378, 675–680.
Kusakabe, M., Ku, T.-L., Southon, J.R., Measures, C.I., 1990. Beryllium isotopes in the ocean. Geochem. J. 24, 263–272.
Kusakabe, M., Ku, T.-L., Southon, J.R., Vogel, J.S., Nelson, D.E., Measures, C.I., Nozaki, Y., 1987. The distribution of 10Be and 9Be in ocean water. Nucl. Instrum. Methods Phys. Res. B29, 306–310.
Lal, D., Peters, B., 1967. Cosmic ray produced radioactivity on the Earth. In: Kosmiche Strahlung II/Cosmic Rays II. Springer, Berlin Heidelberg, pp. 551–612.
Lao, Y., Anderson, R.F., Broecker, W.S., Hofmann, H.J., Wolfli, W., 1993. Particulate fluxes of 230Th, 231Pa, and 10Be in the northeastern Pacific. Ocean 57, 205–217.
Lao, Y., Anderson, R.F., Broecker, W.S., Trumbore, S.E., Hofman, H.J., Wolfli, W., 1992. Increased production of cosmogenic 10Be during the last glacial maximum. Nature 357, 576–578.
Lea, D.W., Pak, D.K., Spero, H.J., 2000. Climate impact of late Quaternary equatorial Pacific sea surface temperature variations. Science 289, 1719–1724, 1979.
Leal, A.L., Anderson, R.F., Bausch, A., Fleisher, M.Q., Singh, S.K., Lao, Y., Chinni, V., Francois, R., 2025. 231Pa/230Th ratios in the Atlantic and Indian oceans and their implications for the application of the ratios as an ocean circulation proxy. Quat. Sci. Rev. 363. https://doi.org/10.1016/j.quascirev.2025.109448.
Lippold, J., Gutjahr, M., Blaser, P., Christner, E., de Carvalho Ferreira, M.L., Mulitza, S., Christl, M., Wombacher, F., Böhm, E., Antz, B., Cartapanis, O., Vogel, H., Jaccard, S. L., 2016. Deep water provenance and dynamics of the (de)glacial Atlantic meridional overturning circulation. Earth Planet Sci. Lett. 445, 68–78. https://doi.org/10.1016/j.epsl.2016.04.013.
Lisiecki, L.E., Raymo, M.E., 2005. A Pliocene-Pleistocene stack of 57 globally distributed benthic δ 18O records. Paleoceanography 20, 1–17. https://doi.org/10.1029/2004PA001071.
Marcantonio, F., Anderson, R.F., Higgins, S., Stute, M., Schlosser, P., Kubik, P., 2001. Sediment focusing in the central equatorial Pacific Ocean. Paleoceanography 16, 260–267. https://doi.org/10.1029/2000PA000540.
Marcantonio, F., Anderson, R.F., Stute, M., Kumar, N., Schlosser, P., Mix, A., 1996. Extraterrestrial 3 He as a tracer of marine sediment transport and accumulation. Nature 383.
Marcantonio, Franco, Kumar, N., Stute, M., Anderson, R.F., Seidl, M.A., Schlosser, P., Mix, A., 1995. A comparative study of accumulation rates derived by He and Th isotope analysis of marine sediments. Earth Planet Sci. Lett. 133, 549–555.
Masarik, J., Beer, J., 2009. An updated simulation of particle fluxes and cosmogenic nuclide production in the Earth's atmosphere. J. Geophys. Res. Atmos. 114, D11103. https://doi.org/10.1029/2008JD010557.
McGee, D., Winckler, G., Borunda, A., Serno, S., Anderson, R.F., Recasens, C., Bory, A., Gaiero, D., Jaccard, S.L., Kaplan, M., McManus, J.F., Revel, M., Sun, Y., 2016. Tracking eolian dust with helium and thorium: impacts of grain size and provenance. Geochim. Cosmochim. Acta 175, 47–67. https://doi.org/10.1016/j.gca.2015.11.023.
McGee, D., Mukhopadhyay, S., 2013. Extraterrestrial He in sediments: from recorder of asteroid collisions to timekeeper of global environmental changes. In: The Noble Gases as Geochemical Tracers. Springer, pp. 155–176.
McHargue, L.R., Damon, P.E., 1991. The global beryllium 10 cycle. Rev. Geophys. 29, 141–158. https://doi.org/10.1029/91RG00072.
McManus, J.F., Francois, R., Gherardi, J.-M., Keigwin, L.D., Brown-Leger, S., 2004. Collapse and rapid resumption of Atlantic meridional circulation linked to deglacial climate changes. Nature 428.
Measures, C.I., Ku, T.L., Luo, S., Southon, J.R., Xu, X., Kusakabe, M., 1996. The Distribution of 10Be and 9Be in the South Atlantic, vol. 43, pp. 987–1009.
Ménabréaz, L., Thouveny, N., Bourlès, D.L., Deschamps, P., Hamelin, B., Demory, F., 2011. The Laschamp geomagnetic dipole low expressed as a cosmogenic 10Be atmospheric overproduction at ~41ka. Earth Planet Sci. Lett. 312, 305–317. https://doi.org/10.1016/j.epsl.2011.10.037.
Middleton, J.L., Mukhopadhyay, S., Costa, K.M., Pavia, F.J., Winckler, G., McManus, J.F., D'Almeida, M., Langmuir, C.H., Huybers, P.J., 2020. The spatial footprint of hydrothermal scavenging on 230ThXS-derived mass accumulation rates. Geochim Cosmochim Acta 272, 218–234. https://doi.org/10.1016/j.gca.2020.01.007.
Middleton, J.L., Mukhopadhyay, S., Langmuir, C.H., McManus, J.F., Huybers, P.J., 2018. Millennial-scale variations in dustiness recorded in Mid-Atlantic sediments from 0 to 70 ka. Earth Planet Sci. Lett. 482, 12–22. https://doi.org/10.1016/j.epsl.2017.10.034.
Murray, R.W., Knowlton, C., Leinen, M., Mix, A.C., Polsky, C.H., 2000. Export production and carbonate dissolution in the central equatorial Pacific Ocean over the past 1 Myr. Paleoceanography 15 (6), 570–592.
Murray, R.W., Leinen, M., Murray, D.W., Mix, A.C., Knowlton, C.W., 1995. Terrigenous Fe Input and biogenic sedimentation in the glacial and interglacial equatorial Pacific-Ocean. Global Biogeochemical Cycles 9 (4), 667–684.
Naafs, B.D.A., Hefter, J., Grützner, J., Stein, R., 2013. Warming of surface waters in the mid-latitude North Atlantic during heinrich events. Paleoceanography 28, 153–163. https://doi.org/10.1029/2012PA002354.

Oppo, D.W., Fairbanks, R.G., 1987. Variability in the deep and intermediate water circulation of the Atlantic Ocean during the past 25,000 years: northern hemisphere modulation of the Southern Ocean. Earth Planet Sci. Lett. 86, 1–15.
Pavia, F.J., Abell, J.T., Middleton, J.L., Leal, A., Vivancos, S.M., Fleisher, M.Q., Winckler, G., Anderson, R.F., 2024. Discrepant mass accumulation rates of sediments in the South Pacific Ocean from 230Th and 3He measurements. Geochim Cosmochim Acta 365, 215–228. https://doi.org/10.1016/j.gca.2023.11.019.
Pöppelmeier, F., Jeltsch-Thömmes, A., Lippold, J., Joos, F., Stocker, T.F., 2023. Multi-proxy constraints on Atlantic circulation dynamics since the last ice age. Nat. Geosci. 16, 349–356. https://doi.org/10.1038/s41561-023-01140-3.
Rafter, P.A., Gray, W.R., Hines, S.K.V., Burke, A., Costa, K.M., Gottschalk, J., Hain, M.P., Rae, J.W.B., Southon, J.R., Walczak, M.H., Yu, J., Adkins, J.F., Devries, T., 2022. Global reorganization of deep-sea circulation and carbon storage after the last ice age. Sci. Adv. 8, 5434.
Raisbeck, G.M., Yiou, F., Bourles, D., Kent, D.V., 1985. Evidence for an increase in cosmogenic 10Be during a geomagnetic reversal. Nature 315, 315–317.
Rutberg, R.L., Hemming, S.R., Goldstein, S.L., 2000. Reduced North Atlantic deep water flux to the glacial Southern Ocean inferred from neodymium isotope ratios. Nature 405, 935–938.
Rutsch, H.-J., Mangini, A., Bonani, G., Dittrich-Hannen, B., Kubik, P.W., Suter, M., Segl, M., 1995. 10Be and Ba concentrations in West African sediments trace productivity in the past. Earth Planet Sci. Lett. 133, 129–143.
Savranskaia, T., Egli, R., Simon, Q., Valet, J.-P., Bassinot, F., Thouveny, N., 2024. Removing climatic overprints in sedimentary cosmogenic beryllium records: potentials and limits. G-cubed 25. https://doi.org/10.1029/2024GC011761 e2024GC011761.
Savranskaia, T., Egli, R., Valet, J.P., Bassinot, F., Meynadier, L., Bourlès, D.L., Simon, Q., Thouveny, N., 2021. Disentangling magnetic and environmental signatures of sedimentary 10Be/9Be records. Quat. Sci. Rev. 257, 106809. https://doi.org/10.1016/j.quascirev.2021.106809.
Sayles, F.L., Martin, W.R., Chase, Z., Anderson, R.F., 2001. Benthic remineralization and burial of biogenic SiO2, CaCO3, organic carbon, and detrital material in the Southern Ocean along a transect at 170° west. Deep-Sea Research II 48, 4323–4383.
Segl, M., Mangini, A., Beer, J., Bonani, G., Suter, M., Wölfli, W., Measures, C., 1987. 10Be in the Atlantic Ocean, A transect at 25°N. Nucl. Instrum. Methods Phys. Res. B29, 332–334.
Sellén, E., Jakobsson, M., Frank, M., Kubik, P.W., 2009. Pleistocene variations of beryllium isotopes in central Arctic Ocean sediment cores. Glob Planet Change 68, 38–47. https://doi.org/10.1016/j.gloplacha.2009.03.024.
Simon, Q., Thouveny, N., Bourlès, D.L., Valet, J.P., Bassinot, F., 2020. Cosmogenic 10Be production records reveal dynamics of geomagnetic dipole moment (GDM) over the Laschamp excursion (20–60 ka). Earth Planet Sci. Lett. 550. https://doi.org/10.1016/j.epsl.2020.116547.
Simon, Q., Thouveny, N., Bourlès, D.L., Nuttin, L., Hillaire-Marcel, C., St-Onge, G., 2016a. Authigenic 10Be/9Be ratios and 10Be-fluxes (230Thxs-normalized) in central Baffin Bay sediments during the last glacial cycle: paleoenvironmental implications. Quat. Sci. Rev. 140, 142–162. https://doi.org/10.1016/j.quascirev.2016.03.027.
Simon, Q., Thouveny, N., Bourlès, D.L., Valet, J.P., Bassinot, F., Ménabréaz, L., Guillou, V., Choy, S., Beaufort, L., 2016b. Authigenic 10Be/9Be ratio signatures of the cosmogenic nuclide production linked to geomagnetic dipole moment variation since the Brunhes/Matuyama boundary. J. Geophys. Res. Solid Earth 121, 7716–7741. https://doi.org/10.1002/2016JB013335.
Smith, M., Glick, E., Lodestro, S., Rashid, H., 2013. Data report: oxygen isotopes and foraminifer abundance record for the last glacial-interglacial cycle and marine isotope stage 6 at IODP U1313. Proceedings of Integrated Ocean Drilling Program 303, 306.
Suganuma, Y., Okuno, J., Heslop, D., Roberts, A.P., Yamazaki, T., Yokoyama, Y., 2011. Post-depositional remanent magnetization lock-in for marine sediments deduced from 10Be and paleomagnetic records through the Matuyama-Brunhes boundary. Earth Planet Sci. Lett. 311, 39–52. https://doi.org/10.1016/j.epsl.2011.08.038.
Valet, J.P., Savranskaia, T., Egli, R., Simon, Q., Bassinot, F., Thouveny, N., 2024. Beryllium ten production and relative paleointensity for the past 1.2 million years. Quat. Sci. Rev. 344. https://doi.org/10.1016/j.quascirev.2024.108993.
Valet, J.P., Meynadier, L., Guyodo, Y., 2005. Geomagnetic dipole strength and reversal rate over the past two million years. Nature 435, 802–805. https://doi.org/10.1038/nature03674.
Valletta, R.D., Willenbring, J.K., Passchier, S., Elmi, C., 2018. 10Be/9Be ratios reflect antarctic ice sheet freshwater discharge during Pliocene warming. Paleoceanogr. Paleoclimatol. 33, 934–944. https://doi.org/10.1029/2017PA003283.
von Blanckenburg, F., O'Nions, R.K., 1999. Response of beryllium and radiogenic isotope ratios in Northern Atlantic Deep Water to the onset of northern hemisphere glaciation. Earth Planet Sci Lett 167, 175–182.
von Blanckenburg, F., O'Nions, R.K., Belshaw, N.S., Gibb, A., Hein, J.R., 1996. Global distribution of beryllium isotopes in deep ocean water as derived from Fe-Mn crusts. Earth Planet Sci. Lett. 141, 213–226.
Waelbroeck, C., Pichat, S., Böhm, E., Lougheed, B.C., Faranda, D., Vrac, M., Missiaen, L., Vazquez Riveiros, N., Burckel, P., Lippold, J., Arz, H.W., Dokken, T., Thil, F., Dapoigny, A., 2018. Relative timing of precipitation and ocean circulation changes in the Western equatorial Atlantic over the last 45 kyr. Clim. Past 14, 1315–1330. https://doi.org/10.5194/cp-14-1315-2018.
Wagner, G., Masarik, J., Beer, J., Baumgartner, S., Imboden, D., Kubik, P.W., Synal, H.-A., Suter, M., 2000. Reconstruction of the geomagnetic field between 20 and 60 kyr BP from cosmogenic radionuclides in the GRIP ice core. Nucl. Instrum. Methods Phys. Res. B 172, 597–604.
Wara, M.W., Ravelo, A.C., Delaney, M.L., 2005. Permanent El nino-like conditions during the Pliocene warm period. Science 309, 758–761. https://doi.org/10.1126/science.1114760, 1979.
White, D.A., Fink, D., Post, A.L., Simon, K., Galton-Fenzi, B., Foster, S., Fujioka, T., Jeromson, M.R., Blaxell, M., Yokoyama, Y., 2019. Beryllium isotope signatures of ice shelves and sub-ice shelf circulation. Earth Planet Sci. Lett. 505, 86–95. https://doi.org/10.1016/j.epsl.2018.10.004.
Willenbring, J.K., von Blanckenburg, F., 2010a. Long-term stability of global erosion rates and weathering during late-cenozoic cooling. Nature 465, 211–214. https://doi.org/10.1038/nature09044.
Willenbring, J.K., von Blanckenburg, F., 2010b. Meteoric cosmogenic Beryllium-10 adsorbed to river sediment and soil: applications for Earth-surface dynamics. Earth Sci. Rev. 98, 105–122. https://doi.org/10.1016/j.earscirev.2009.10.008.
Winckler, G., Anderson, R.F., Schlosser, P., 2005. Equatorial Pacific productivity and dust flux during the mid-pleistocene climate transition. Paleoceanography 20. https://doi.org/10.1029/2005PA001177. PA4025.
Yang, W., Guo, L., Chuang, C.Y., Santschi, P.H., Schumann, D., Ayranov, M., 2015. Influence of organic matter on the adsorption of 210Pb, 210Po and 7Be and their fractionation on nanoparticles in seawater. Earth Planet Sci. Lett. 423, 193–201. https://doi.org/10.1016/j.epsl.2015.05.007.
Yokoyama, Y., Sproson, A.D., 2026. Beryllium isotopes in marine science: understanding Ocean current and ice dynamics. Ann. Rev. Mar. Sci 18, 121–139. https://doi.org/10.1146/annurev-marine-040224.
Zhou, Y., McManus, J.F., Pallone, C.T., Kenna, T.C., Weinstein, G.A., Garcia, H., 2025. Abrupt weakening of deep Atlantic circulation at the last glacial inception. Nat. Commun. 16. https://doi.org/10.1038/s41467-025-62960-y.